

UNIVERSIDADE DE LISBOA
INSTITUTO SUPERIOR TÉCNICO
Università degli Studi di Padova

Tokamak Magnetic Control Simulation: Applications for JT60-SA and ISTTOK Operation.

Doménica Corona Rivera

Supervisor: Prof. Horácio Fernandes

Co-Supervisor: Prof. Nuno Cruz

External supervisor: Prof. Alfredo Pironti

Thesis specifically prepared to obtain the PhD Degree in
Technological Physics Engineering

Month 2020

ABSTRACT

Abstract en ingles

Keywords:Real-time control, plasma current, centroid position, state-space

RESUMO

Abstract em tuga

Palavras-chave:

SOMMARIO

Abstract em italiano

Parole chiave:

ACKNOWLEDGEMENTS

This work was supported by Fundação para a Ciência e a Tecnologia (FCT) under the grant No.**PD/BD/114306/2016** carried out as part of the training in the framework of the Advanced Program in Plasma Science and Engineering (APPLAuSE, sponsored by FCT under grant No. PD/00505/2012).

CONTENTS

1	INTRODUCTION	3
1.1	Tokamak plasma control	3
1.2	Behind the plasma current	3
1.3	Thesis outline	3
2	PLASMA CONTROL SYSTEMS	5
2.1	Overview of control systems	5
2.1.1	DIII-D Plasma Control System	5
2.1.2	Système de Contrôle Distribué	7
2.2	MARTe framework	7
2.2.1	MARTe architecture	8
2.2.2	Hardware containers	8
2.2.3	MARTe 2.0	9
2.3	Equilibrium and control algorithms	9
2.3.1	State-Space models	9
2.3.2	PID control	9
2.3.3	Multiple-Input Multiple-Output control	9
3	JT60-SA CONTROL DESIGN	11
3.1	Machine description	11
3.2	CREATE magnetic reconstruction tools	13
3.3	Controller design	13
3.4	QST reconstruction and control implementation	16
3.4.1	Cauchy Condition Surface reconstruction method	17
3.4.2	QST magnetic controller (FBC)	18
3.5	Simulation results	19
3.5.1	Disturbances	19
3.5.2	Gap-based XSC	21
3.5.3	Isoflux XSC and QST controller	25
3.5.4	Shape reference change	28
4	ISTTOK	35
4.1	Machine description	35
4.2	Diagnostics and Actuators	35
4.3	ATCA-MIMO-ISOL boards	35

Contents

4.3.1	Hardware layout	35
4.3.2	Real-time integration software	35
4.4	Plasma current magnetic field	35
4.5	Plasma centroid position determination	35
5	ISTTOK RESULTS	37
5.1	Implementation of the General Application Modules	37
5.1.1	PID control implementation	37
5.1.2	Data-driven state-space model retrieving	37
5.1.3	Kalman filter implementation	37
5.1.4	Multiple-Input Multiple-Output control implementation	37
5.2	Plasma curruent centroid position control results	37
5.2.1	PID control and LQR control results	43
6	CONCLUSIONS	47
	Bibliography	51
A	EXTENDED CONTROL RESULTS	53
B	FBC CONTROLLER AND CCS CONFIGURATION	67

LIST OF FIGURES

Figure 2.1	DIII-D digital PCS in 1991 [2].	6
Figure 2.2	Actual DIII-D PCS real-time systems [4].	6
Figure 2.3	TCV SCD. Real-time network nodes connection. The nodes configurations are shown together with the typical diagnostic and actuator systems to which they are connected [7].	7
Figure 2.4	Example of a set of GAMs connected to the DDB. Timing and hardware GAMs provide the I/O interface to the exterior, whereas a generic waveform GAM inputs the reference for a PID controller. Finally, the output is sent to a DAC and the data is stored for analysis by a collection GAM. It should be noticed that the reference generation and the controller GAM are not aware of the changes in the data providers and data consumers. [11]	8
Figure 3.1	JT60-SA tokamak configuration and its main elements [15].	11
Figure 3.2	JT-60SA poloidal cross-section and layout of the Poloidal Field coils system [16].	12
Figure 3.3	LCFS Equilibria corresponding to the different Scenario 2 snapshots: X-point formation (XPF), Start of Heating(SOH), the Start of Flattop (SOF), End of Flattop (EOF), End Of Cooling(EOC) and End of Currents in the PF coils (EOC) [17].	13
Figure 3.4	Poloidal cross-section of the JT-60SA plasma at the Start of the Flat Top (SOF) for reference Scenario 2. At SOF, the nominal plasma current is 5.5 MA, while the nominal values for poloidal beta β_p and internal inductance l_i are 0.53 and 0.85, respectively.	14
Figure 3.5	Poloidal cross-section of the JT-60SA plasma at the Start of the Flat Top (SOF) for reference Scenario 2. At SOF, the nominal plasma current is 5.5 MA, while the nominal values for poloidal beta β_p and internal inductance l_i are 0.53 and 0.85, respectively. In this figure the 85 gaps used to assess the plasma shape controller performance are shown.	15
Figure 3.6	SOF equilibrium reconstructed from CREATE-NL and the CCS code along with the magnetic field and flux sensors locations.	17
Figure 3.7	JT-60SA overall control scheme with the CREATE linearized model and the CCS LCFS reconstruction method using the XSC for an isoflux control approach.	20

List of Figures

- Figure 3.8 Isoflux control JT-60SA overall scheme with a block for the CREATE JT60-SA linearized model, a block for reconstructing the magnetic fluxes with the CCS method and the QST controller. 20
- Figure 3.9 Poloidal beta and internal inductance time traces for Disturbance #1 that models the expected disturbance soon after the plasma current flattop is reached (at $t \sim 20$ s), according to what has been considered in [28]. 21
- Figure 3.10 Poloidal beta and internal inductance time traces for Disturbance #2 that models the behavior of these variables due to the presence of a compound ELM as defined in [17]. 22
- Figure 3.11 Poloidal beta and internal inductance time traces for Disturbance #3 that models the behavior of these variables due to the presence of a minor disruption as defined in [17]. 23
- Figure 3.12 Different choices for the set of controlled gaps used for gap controller. 24
- Figure 3.13 RMSE time traces for the different gaps selections in the presence of Disturbance #2 (compound ELMs). For all the considered cases, the RMSE is computed on the set of 85 gaps shown in figure 3.5. 24
- Figure 3.14 RMSE time traces for the different gaps selections in the presence of Disturbance #3 (minor disruption). For all the considered cases, the RMSE is computed on the set of 85 gaps shown in Fig. 3.5. 25
- Figure 3.15 Comparison of the shape controller performance in the presence of Disturbance #3 (minor disruption). The two cases of 8 and 20 gaps are considered. 26
- Figure 3.16 LCFS reconstructed by CREATE and the CCS code for the JT60-SA scenario 2 SOF equilibrium with a Minor disruption at steady-state for the three considered selection of control segments using the XSC with an isoflux approach. 27
- Figure 3.17 CREATE-NL JT60-SA Scenario 2 - SOF equilibrium compared with the LCFS reconstructed by the CCS method for 8 control points in the presence of a Minor disruption at steady-state using both the XSC and the QST control. 28
- Figure 3.18 CREATE-NL JT60-SA Scenario 2 - SOF equilibrium compared with the LCFS reconstructed by the CCS method for 8 control points in the presence of a Minor disruption (Disturbance #3) at the time of maximum deviation for both cases. As shown in figure 3.11, the disturbance occurs at $t \sim 20$ s 29
- Figure 3.19 Comparison between the flux at the X-point and the fluxes in the 8 control points reconstructed by the CCS method, when a Minor disruption is applied at $t=20$ s using the XSC and the QST controller. It should be noticed that QST control has a faster performance to reach the steady-state and less error. 29

Figure 3.20	Flux errors for the case of 8 control points in the presence of a Minor disruption using the XSC and the QST controller. Even though both controllers reject the disturbance, is possible to remark how the QST control has an overall smaller error.	30
Figure 3.21	XSC isoflux response to a change of shape request. The dashed black shape is the starting shape, while the red one is the target shape. The magenta dashed shape is the LCFS at steady state.	32
Figure 3.22	Comparison between the flux at the X-point and the fluxes a	32
Figure 3.23	Flux control error for the case of 8 control points for a change in the shape reference between 20 and 21.5 s.	33
Figure 5.1	ISTTOK MARTe overall control position scheme	38
Figure 5.2	Fig.	38
Figure 5.3	Fig.	39
Figure 5.4	Pole-Zero maps in closed loop for the model when $I_p \approx 4kA$. Superposition of poles and zeros can be seen in the four transfer functions.	39
Figure A.1	Plasma centroid position Shot# 48563 Shot# 48561	54
Figure A.2	lalala Shot# 48563 Shot# 48561	54
Figure A.3	Plasma centroid position Shot# 48556 Shot# 48552	55
Figure A.4	lalala Shot# 48556 Shot# 48552	55
Figure A.5	Plasma centroid position Shot# 48551 Shot# 48554	56
Figure A.6	lalala Shot# 48551 Shot# 48554	56
Figure A.7	Plasma centroid position Shot# 48515 Shot# 48541	57
Figure A.8	lalala Shot# 48515 Shot# 48541	57
Figure A.9	Plasma centroid position Shot# 48544 Shot# 48542	58
Figure A.10	lalala Shot# 48544 Shot# 48542	58
Figure A.11	Plasma centroid position Shot# 48546 Shot# 48548	59
Figure A.12	lalala Shot# 48546 Shot# 48548	59
Figure A.13	Plasma centroid position Shot# 48340 Shot# 48338	60
Figure A.14	lalala Shot# 48340 Shot# 48338	60
Figure A.15	Plasma centroid position Shot# 48343 Shot# 48342	61
Figure A.16	lalala Shot# 48343 Shot# 48342	61
Figure A.17	Plasma centroid position Shot# 48346 Shot# 48345	62
Figure A.18	lalala Shot# 48346 Shot# 48345	62
Figure A.19	Plasma centroid position Shot# 48349 Shot# 48348	63
Figure A.20	lalala Shot# 48349 Shot# 48348	63
Figure A.21	Plasma centroid position Shot# 48352 Shot# 48354	64
Figure A.22	lalala Shot# 48352 Shot# 48354	64

List of Figures

Figure A.23	Plasma centroid position Shot# 48351 Shot# 48350	65
Figure A.24	lalala Shot# 48351 Shot# 48350	65

LIST OF TABLES

Table 3.1	Steady-state RMSE values for the different choices of number of controlled gaps and for the different disturbances test cases.	23
Table 3.2	Steady-state flux RMSE values for the different selection of control points for the JT60-SA scenario 2, SOF equilibrium in the presence of Disturbance #1 at $t \sim 20$ s.	27
Table 3.3	X-point position steady state error for JT60-SA scenario 2, SOF equilibrium in the presence of Disturbance #1 at $t \sim 20$ s. The XSC and QST controller were used in different simulations for the shape control along with two reconstruction methods for the LCFS.	30
Table 3.4	Steady-state flux RMSE values for the different selection of control points for the JT60-SA scenario 2, SOF equilibrium in the presence of Disturbance #2 (Compound ELM) at $t \sim 20$ s.	30
Table 3.5	X-point position steady state error for JT60-SA scenario 2, SOF equilibrium in the presence of Disturbance #2 (Compound ELM) at $t \sim 20$ s. The XSC and QST controller were used in different simulations for the shape control along with two reconstruction methods for the LCFS.	31
Table 3.6	Steady-state flux RMSE values for the different selection of control points for the JT60-SA scenario 2, SOF equilibrium in the presence of Disturbance #3 (Minor disruption) at $t \sim 20$ s.	31
Table 3.7	X-point position steady state error for JT60-SA scenario 2, SOF equilibrium in the presence of Disturbance #3 (Minor disruption) at $t \sim 20$ s. The XSC and QST controller were used in different simulations for the shape control along with two reconstruction methods for the LCFS.	31
Table 5.1	Centroid position RMSE comparison between PID and MIMO-LQR controlled discharges for different set points and plasma current scenarios.	44

LIST OF ABBREVIATIONS

@TODO: Review variable lists as writing the thesis

- AC - Alternating Current
- ADC - Analog to Digital Converter
- ATCA - Advanced Telecommunications Computing Architecture
- CREATE - Consorzio di Ricerca per l'Energia, l'Automazione e le Tecnologie dell'Elettromagnetismo
- DAC - Digital to Analog Converter
- EO - Electronic Offset
- GAM - Generic Application Module
- IST - Instituto Superior Técnico
- LCFS- Last Closed Flux Surface
- LQR - Linear Quadratic Regulator
- MARTe - Multi-threaded Application Real-Time executor
- MIMO - Multiple-Input Multiple-Output
- PCS - Plasma Control System
- PF - Poloidal Field
- PID - Proportional - Integrative - Derivative
- QST - Quantum
- RFM - Reflective Memory
- RMSE - Root Mean Squared Error
- SCD - Système de Contrôle Distribué
- SOF - Start Of Flattop
- XSC - eXtreme Shape Controller
- WO - Wiring Offset

LIST OF VARIABLES

@TODO: Review variable lists as writing the thesis

VARIABLES:

- I_p - Plasma current
- B_p - Poloidal magnetic field
- μ_0 - Vacuum permeability
- β_p - Poloidal beta
- l_i - Internal inductance

1

INTRODUCTION

1.1 TOKAMAK PLASMA CONTROL

1.2 BEHIND THE PLASMA CURRENT

1.3 THESIS OUTLINE

2

PLASMA CONTROL SYSTEMS

2.1 OVERVIEW OF CONTROL SYSTEMS

The control of plasma position, shape and current among other parameters is one of the crucial engineering problems for present and future magnetic confinement devices. The Plasma Control Systems (PCS) lead with the overall control of fusion devices being responsible also for the plasma configuration and scenarios algorithms [1, Chapter 8]. Currently different PCS's are use in the tokamaks around the world. In this chapter the "DIII-D-like" PCS, the Système de Contrôle Distribué (SCD) and the Multi-threaded Application Real-Time executor (MARTe) will be approach, this last one being of special interest due to its extensive utilization in this work.

2.1.1 *DIII-D Plasma Control System*

The DIII-D-like PCS is use in various fusion research facilities such as EAST(China), K-STAR (South Korea) and MAST (UK). Early documentation regarding the PCS in DIII-D¹ reefers to digitalization of analog signals transmitted to a high speed processor executing a shape control algorithm and then writing the result to a digital to analog converter for driving the controlled systems . The real-time computer used allowed to performed operations with vectors and matrices required for the plasma shape control algorithm [2]. Figure 2.1 shows the block diagram of the DIII-D PCS 30 years ago.

In recent years the DIII-D PCS had extensive software and hardware upgrades. The PCS actual software consists of an infrastructure library core which provides all the routines that are necessary for implementing a basic and generic control system. The current PCS hardware configuration uses a collection of Intel Linux based multi-processor computers running in parallel to perform the real-time analysis and feedback control [3]. New digitizers have been added to the real-time network to increase the number of signals acquired an to control hardware on real-time, several real-time control algorithms were added and real-time data was added to external entities such as web server. [4]. In

¹ DIII-D is a D-shape tokamak operated by General Atomics in San Diego, California.

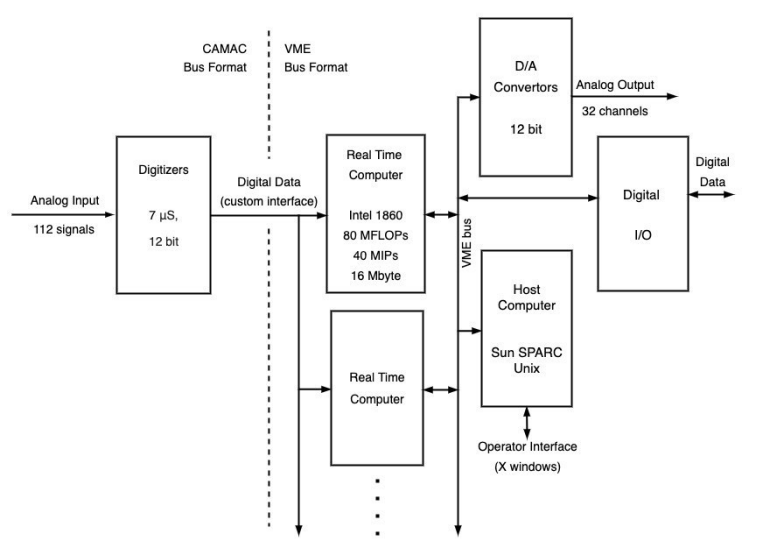


Figure 2.1.: DIII-D digital PCS in 1991 [2].

the current version of the PCS, a Myricom² network has been replaced with a 40 Gb/sec InfiniBand³ network based on the Mellanox Connect-X 3⁴ hardware set. Figure 2.2 shows the currently overall networking diagram of DIII-D PCS .

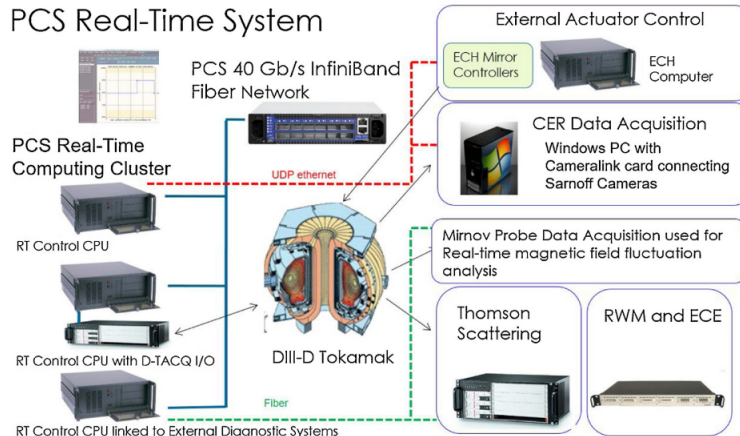


Figure 2.2.: Actual DIII-D PCS real-time systems [4].

² Myricom networks also called Myrnet are high speed networking systems used to interconnect machines to form computer clusters.

³ Is a network architecture from Mellanox designed to support I/O connectivity and reliability, availability, and serviceability Internet requirements [5].

⁴ The Connect-X from the Mellanox company are Ethernet network interface cards with PCI Express.

2.1.2 Système de Contrôle Distribué

The TCV⁵ distributed control system uses a modular network of real time PC nodes liken by a real time network to provide feedback control over all of the actuator systems. Each node consists of a Linux PC either embedded on a Compact-PCI module or as a desktop computer with Intel CPU. A fiber optic ring network links the reflective memory (RFM) network cards in each node [6]. The design of the diagnostic signal processing and control algorithms is performed in Matlab-Simulink software. During the real-time execution C/C++ code is generated from the Simulink and compiled into a Linux shared library and distributed to target nodes providing the input/output interface to the control algorithm code [7]. Figure 2.3 depicts the TCV SCD layout with the connectivity to diagnostics and actuators.

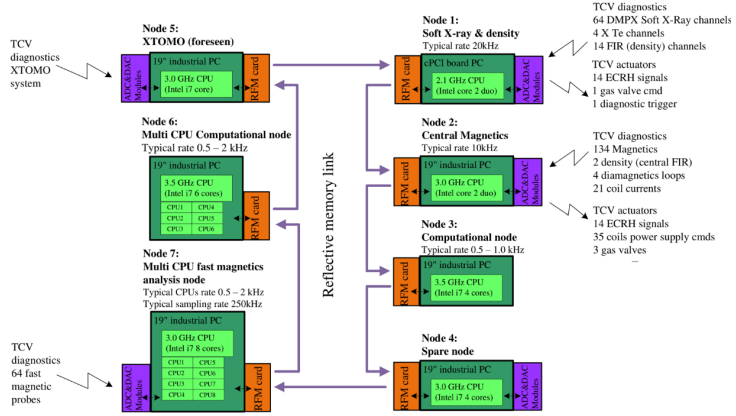


Figure 2.3.: TCV SCD. Real-time network nodes connection. The nodes configurations are shown together with the typical diagnostic and actuator systems to which they are connected [7].

2.2 MARTE FRAMEWORK

Regardless the nature of a real-time system the design of it is usually related to the specific requirements it has, commonly this implies to have customized hardware and software which causes a lack in modularity and portability. When systems become bigger is convenient to provide a common library containing shareable functionalities and which also allows for modular implementations. In order to deal with this the MARTE framework was designed about a decade ago. MARTE was developed in order to standardize general real-time control systems for the execution of control algorithms and is based on a multiplatform C++ library [8]. Previous implementations for a software framework similar to MARTE were developed some years before for the JET tokamak. JETRT was a software framework used to develop real-time control and data acquisition systems which laid the foundation for current MARTE framework [9]. MARTE is currently used in several tokamaks such as JET, FTU, COMPASS and ISTTOK.

⁵ The Tokamak à configuration variable (TCV) is a medium size tokamak localized in Laussane, Switzerland. It is characterized by a highly elongated, rectangular vacuum vessel.

2.2.1 MARTe architecture

The unitary MARTe component is the Generic Application Module (GAM), each of the C++ programmed GAMs usually performs an specific task of the control system, the collection of interconnecting GAMs builds MARTe [10]. The GAMs have an entry point to receive data driven configuration and a set of input and output channels to interface with other GAMs. The Dynamic Data Buffer (DDB) is a generic memory data bus where each GAM receives and produce data using DDB named channels. Usually each GAM is associated with a special function of the system like processing data of an specific diagnostic or perform some control algorithm. MARTe hardware data interface and synchronization for inputs and outputs is performed using a special GAM called IOGAM .

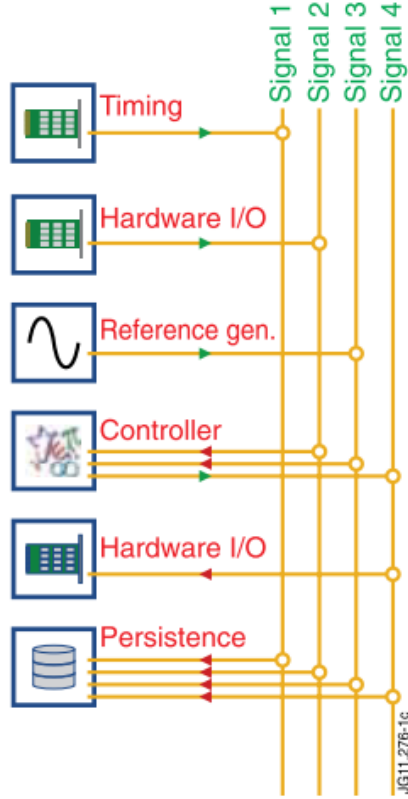


Figure 2.4.: Example of a set of GAMs connected to the DDB. Timing and hardware GAMs provide the I/O interface to the exterior, whereas a generic waveform GAM inputs the reference for a PID controller. Finally, the output is sent to a DAC and the data is stored for analysis by a collection GAM. It should be noticed that the reference generation and the controller GAM are not aware of the changes in the data providers and data consumers. [11]

2.2.2 Hardware containers

The MARTe hardware containers

2.2.3 MARTe 2.0

Software Quality Assurance (QA) processes are being applied to the development of a new version of the MARTe framework also called MARTe 2.0.

[12]

2.3 EQUILIBRIUM AND CONTROL ALGORITHMS

The RAPTOR (RApid Plasma Transport simulatOR) code is a model-based control-oriented code that predicts tokamak plasma profile evolution on real-time. [13]

2.3.1 *State-Space models*

2.3.2 *PID control*

Proportional-Integral-Derivative (PID) control

2.3.3 *Multiple-Input Multiple-Output control*

Multiple-Input Multiple-Output (MIMO)

3

JT60-SA CONTROL DESIGN

3.1 MACHINE DESCRIPTION

JT60-SA is an under-construction superconductive tokamak located at one of the facilities from the National Institutes for Quantum and Radiological Science and Technology (QST) at Naka, Japan whose principal purpose is the contribution to early realization of fusion energy by supporting the exploitation and resolving key physics for the ITER reactor. Figure 3.1 shows the overall general configuration and the most remarkable elements of the machine. The JT-60SA vacuum chamber will have a major radius of 2.96 m and a minor radius of 1.18 m with an overall plasma volume of 132 m^3 [14].

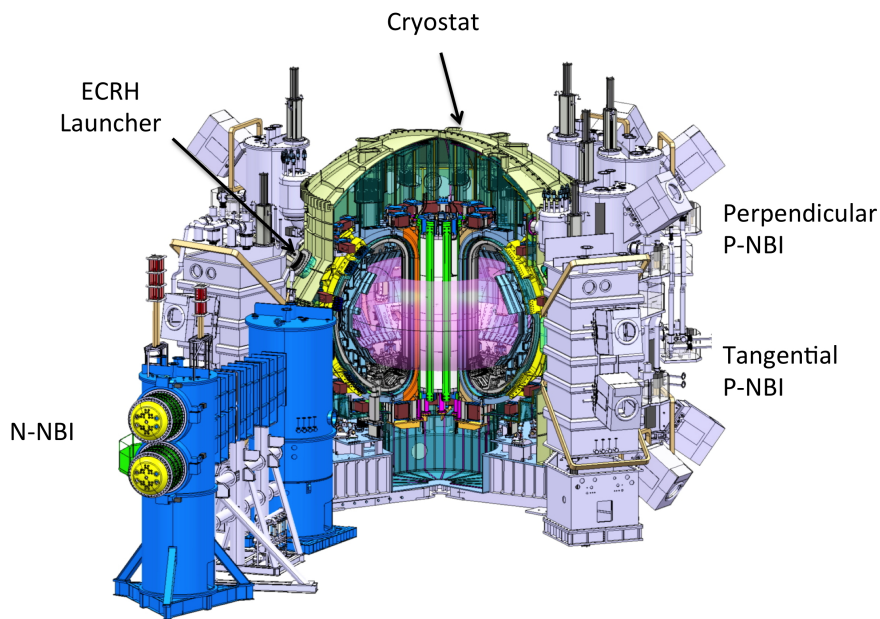


Figure 3.1.: JT60-SA tokamak configuration and its main elements [15].

The Poloidal Field (PF) coils shown in JT60-SA cross-section from figure 3.2 consist of two sets of superconductive coils: the Equilibrium Field Coils (EF1–6) and the Central Solenoid (consisting of four independent coils, named CS1–4). Furthermore, two in-vessel Fast Plasma Position Copper Coils

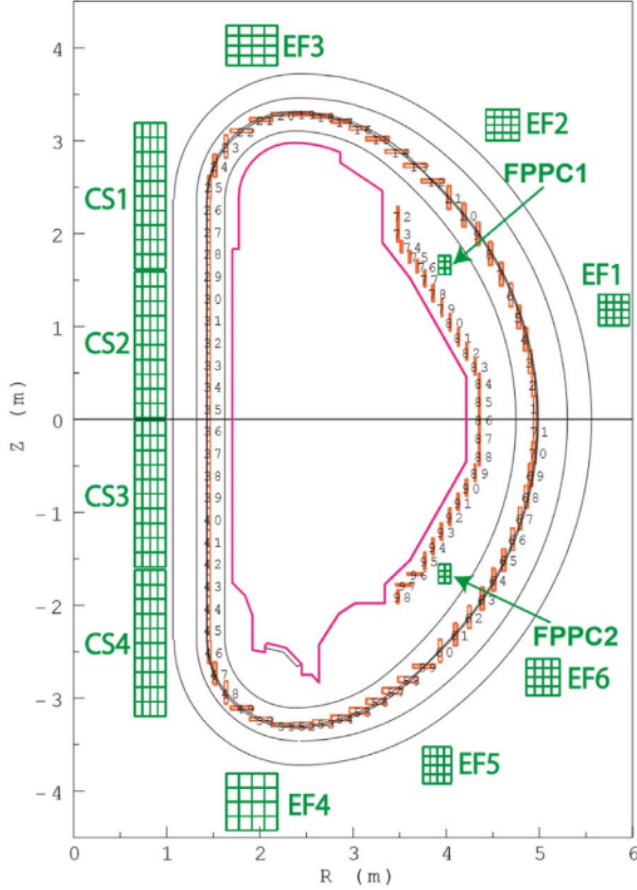


Figure 3.2.: JT-60SA poloidal cross-section and layout of the Poloidal Field coils system [16].

(FPPC1–2) will also be installed [16]. The total of 12 PF coils have independent power sources for the control of the plasma current, position and shape.

JT-60SA shall be capable of investigating different design scenarios. As referred in [17] it exists a set of 6 reference scenarios, additional ones, including some with a shorter repetition rate will be defined in future. For the control study in this section all simulations will be built based on the Scenario 2 characteristics. In particular, Scenario 2 refers to a 5.5 MA inductive lower single null discharge. The Scenario 2 is divided in 5 time snapshots with different equilibrium each one starting at $t=-40$ s until $t=177.96$ s. The different Last Closed Flux Surfaces (LCFS) for each time window are shown in figure 3.3, the time sequence starts at the X-point formation (XPF) followed by the Start of Heating(SOH), the Start of Flattop (SOF), End of Flattop (EOF), End Of Cooling(EOC) and finishing with the End of Currents in the PF coils (EOC). In this section, reconstruction methods and control algorithms will be based on the *Start of Flattop* (SOF) equilibrium shown in figure 3.4. The nominal values for the plasma current, the poloidal beta and the internal inductance for Scenario 2 at SOF are $I_{peq} = 5.5$ MA, $\beta_{peq} = 0.53$, and $l_{eq} = 0.85$.

This chapter will address two different approaches for the LCFS reconstruction along with different plasma current, shape and position controllers for JT60-SA in order to achieve and maintain the desired

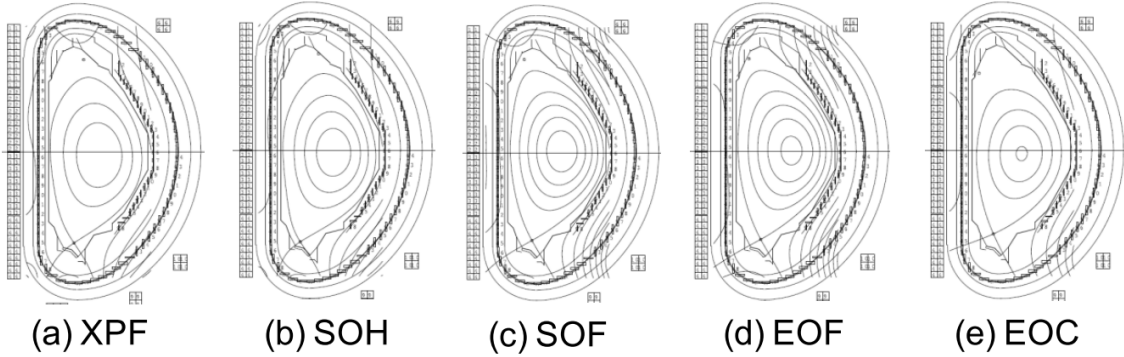


Figure 3.3.: LCFS Equilibria corresponding to the different Scenario 2 snapshots: X-point formation (XPF), Start of Heating(SOH), the Start of flattop (SOF), End of flattop (EOF), and End Of Cooling(EOC) [17].

operational scenario given the plasma equilibrium in the SOF while the performance of the controllers is compared .

3.2 CREATE MAGNETIC RECONSTRUCTION TOOLS

CREATE-NL (Consorzio di Ricerca per l' Energia, l' Automazione e le Tecnologie dell' Elettromagnetismo) is a finite elements method (FEM¹) solver implemented on MATLAB. It deals with the free boundary dynamic plasma equilibrium problem i.e. the MHD (Magneto-Hydro-Dynamics) time evolution of 2D axisymmetric plasmas in tokamaks, including eddy currents in the passive structures, and feedback control laws for current, position and shape control [18].

Using the CREATE codes [18,19] it is possible to retrieve a linearized state-space model that describes the plasma magnetic behavior around that equilibrium².It should be noted that CREATE-NL equilibrium solver has been validated on several tokamaks such as JET and EAST. A JT60-SA CREATE-NL electromagnetic linear model around the equilibrium from the Scenario 2- SOF for the plasma-circuit response has been used for designing the controller presented in next section.

3.3 CONTROLLER DESIGN

The JET (Joint European Torus) tokamak was the first machine where around 2005 a new model based plasma current and shape controller was set up and tested with the existing active circuits and control hardware. The novelty controller was the eXtreme Shape Controller (XSC) and its aim was to

¹ It is well known that many physical and engineering systems are expressed in terms of partial differential equations which cannot be solved via analytical methods. One of the most recurrent techniques is numerical discretization to approximate the solution of the partial differential equations, the FEM is commonly used to solve these approximations in two or three space variables, in this particular case for a numerical solution of the well-known Grad-Shafranov equation.

² Reference [16, Sec. 3] can be consulted for more details about the use of the CREATE equilibrium codes to retrieve plasma linearized models.

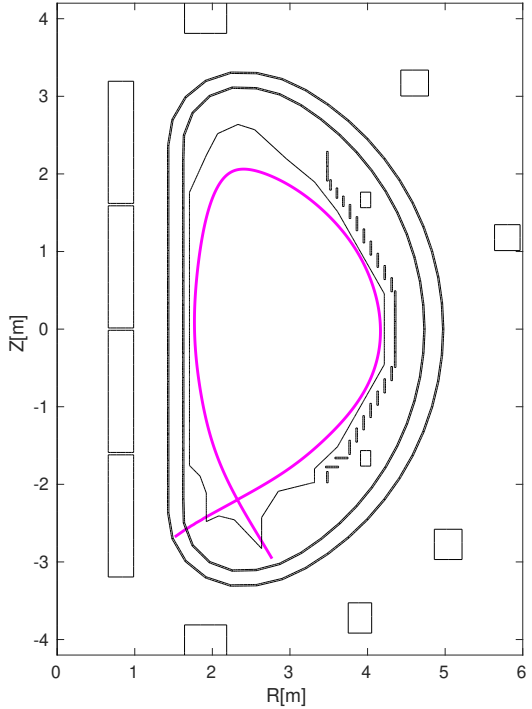


Figure 3.4.: Poloidal cross-section of the JT-60SA plasma at the Start of the Flat Top (SOF) for reference Scenario 2. At SOF, the nominal plasma current is 5.5 MA, while the nominal values for poloidal beta β_p and internal inductance l_i are 0.53 and 0.85, respectively.

improve the performance of the, back then, present controller to allow the control of extremely shaped plasmas with higher values of elongation and triangularity [20]. More recently this control approach was utilized at TCV [21]. At JET, the XSC recently enabled the control of high triangularity shapes with both strike points in the divertor corner, which has a large impact in the H-mode confinement in the case of the ITER-like wall at JET [22].

Usually the controlled shape geometrical descriptors are the distances between the plasma boundary and the vessel at some specific points. These plasma-wall distances are called gaps [23]. The gaps are segments that can be used to describe the shape of the plasma boundary. Being g_i the abscissa along the i -th control segment, we assume that $g_i = 0$ at the first wall. *Gap-based* plasma shape control is achieved by controlling to zero the difference $g_{i\text{ref}} - g_i$ on a sufficiently large number of gaps, being $g_{i\text{ref}}$ the value of the abscissa on the i -th control segment for the reference shape. Figure 3.5 shows a poloidal cross-section of JT-60SA together with a set of 85 gaps used for the assessment of the plasma shape control.

The XSC algorithm can be used either to implement a gap-based control strategy, or an isoflux one, as it has been proposed in [16]. The isoflux strategy consists in controlling the X-point position along with a set of flux differences between the flux at some selected control points along the desired plasma

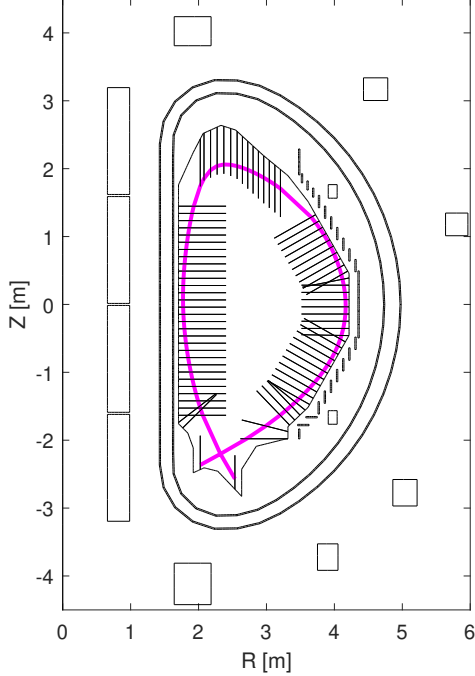


Figure 3.5.: Poloidal cross-section of the JT-60SA plasma at the Start of the Flat Top (SOF) for reference Scenario 2. At SOF, the nominal plasma current is 5.5 MA, while the nominal values for poloidal beta β_p and internal inductance l_i are 0.53 and 0.85, respectively. In this figure the 85 gaps used to assess the plasma shape controller performance are shown.

boundary and the X-point flux. Thus the XSC block inputs are the error between the X-point flux and the fluxes in the control points, and the X-point position error.

The peculiarity of the XSC approach is that it permits to control a number of plasma shape descriptors that is greater than the number of available actuators, i.e. of PF Circuits, this is basically tackled by using a singular value decomposition (SVD) to identify the principal directions of the algebraic mapping between coil currents and geometrical descriptors [20]. The XSC control relies on the PFC decoupling controller (more details can be found in [16, Section 4.4]), since it is assumed that each PF coil can be treated as an independent single-input-single-output (SISO) channel whose dynamic response is modeled in the Laplace domain by

$$I_{PF_i}(s) = \frac{I_{PF_{ref,i}}(s)}{1 + s\tau_{PF}},$$

where I_{PF_i} and $I_{PF_{ref,i}}$ are the Laplace transform of the measured and reference current in the i -th PFC, respectively, and where it is assumed that all the PFC exhibit the same bandwidth (i.e., they have the same time constant τ_{PF}).

Denoting by $\delta Y(s)$ the Laplace transform of the variations of the n_G shape descriptors to be controlled, it is possible to exploit the CREATE electromagnetic linear model [16] that links the variation of the PFC reference currents $\delta I_{PF_{ref}}$ to $\delta Y(s)$, i.e.

$$\delta Y(s) = C \frac{\delta I_{PF_{ref}}(s)}{1 + s\tau_{PF}},$$

which, at steady-state, implies $\delta Y(s) = C\delta I_{PF_{ref}}(s)$.

If the number of controlled plasma shape descriptors n_G is such that $n_G > n_{PF}$, the XSC computes the additional current references as

$$\delta I_{PF_{ref}} = C^\dagger \delta Y. \quad (3.1)$$

where the matrix C^\dagger denotes the pseudo-inverse of C^3 that can be computed via the singular value decomposition (SVD). As a result, the XSC algorithm minimizes the following steady-state performance index

$$J_{XSC} = \lim_{t \rightarrow +\infty} (\delta Y_{ref} - \delta Y(t))^T (\delta Y_{ref} - \delta Y(t)), \quad (3.2)$$

where δY_{ref} are constant references for the geometrical descriptors. When the SVD of the C matrix is used to minimize (3.2), it may happen that some singular values (depending on the plasma configuration) are one order of magnitude smaller than the others. This fact implies that minimizing the performance index (3.2) retaining all the singular values results in a large control effort at the steady-state, that is a large request on some PFC currents which have only a minor effect on the plasma shape. In order to minimize also the control effort, the additional references (3.1) are generated by using only the $\bar{n} < n_{PF}$ linear combinations of PF currents which are related to the largest singular values of the C matrix. This is achieved by using only the \bar{n} singular values when computing the pseudo-inverse C^\dagger .

Moreover, the PFC current variations given by (3.1) are summed to the scenario currents and sent to the PFC decoupling controller as references to be tracked. It is worth to remark here that the dynamic behavior of the XSC is improved by adding a set of proportional-integral-derivative (PID) controllers on each PF coil channel (see [24] for a complete description of the XSC control scheme).

For the development of this work both approaches of the XSC strategy were studied and simulated for a different number of control points: isoflux and gap-based controllers. In addition, a second controller developed by the QST team was implemented in the simulations, the features of this controller will be detailed in the next section.

3.4 QST RECONSTRUCTION AND CONTROL IMPLEMENTATION

Along with the CREATE tools presented on last section for the reconstruction of the LCFS and the XSC for plasma shape control, a reconstruction code and controller provided by the QST team

³ C is the output matrix from the state-space linearized CREATE model for JT60-SA.

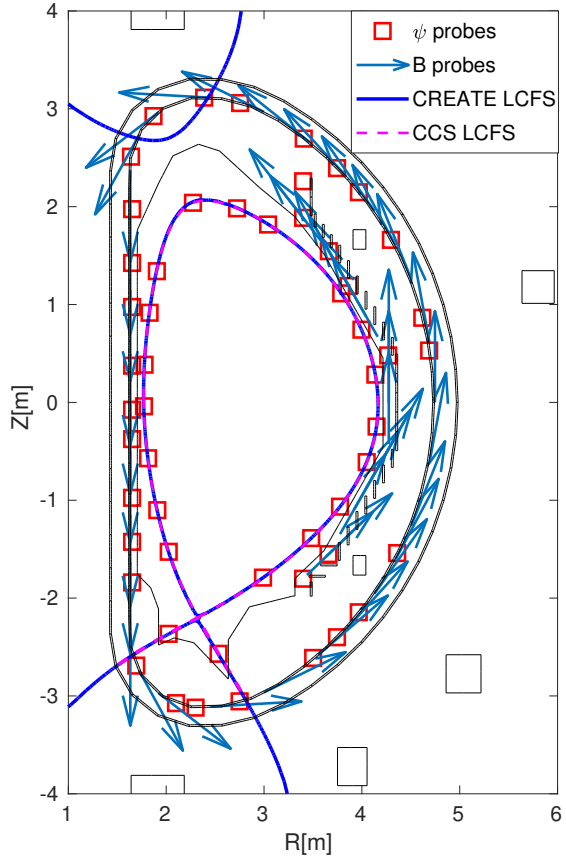


Figure 3.6.: SOF equilibrium reconstructed from CREATE-NL and the CCS code along with the magnetic field and flux sensors locations.

were implemented, tested and compared. This section will briefly describe these two methods and its limitations.

3.4.1 Cauchy Condition Surface reconstruction method

The QST Cauchy Condition Surface (CCS) method for the reconstruction of the magnetic last closed flux surface (LCFS) calculates controlled variables for plasma position and shape control such as the poloidal magnetic flux at control points on an isoflux scheme [25]. The CCS method allows a selection up to 19 geometrical points for describing the LCFS and its input parameters are the current in the PF coils, the measurements in the magnetic field and flux sensors and the plasma current. The output signals from the CCS reconstruction method are the magnetic fluxes at the X-point and at the selected geometrical points.

3.4.2 QST magnetic controller (FBC)

The QST magnetic controller uses the PF coils signals to control the plasma current I_p , position and shape, and the FPPC coils signals for plasma position control. The PF coil currents I_{PF_ref} are calculated using an isoflux control approach using proportional-integral(PI) feedback controllers [26]. The controller calculates I_{PF_ref} reducing $\delta\Psi_s$ and $\delta\Psi_x$ according to:

$$I_{PF_ref}(t + \Delta t) = I_{PF}(t_0) + M_{PF}^\dagger \left[G_{SP}\delta\Psi_s(t) + G_{SI} \int_{t_0}^t \delta\Psi_s(t)dt + G_{XP}\delta\Psi_X(t) + G_{XI} \int_{t_0}^t \delta\Psi_x(t)dt \right], \quad (3.3)$$

where $\delta\Psi_s$ is the residual between the LCFS flux and the control point fluxes, $\delta\Psi_x$ is the difference between the I_p value and its reference, t_0 is the initial time , Δt is the coil control cycle, M_{PF}^\dagger is the ($m \times (n + 1)$) control matrix which is the pseudo-inverse of the Green function M calculated using the SVD method; where m is the number of PF coils , n is the number of control points including the evaluated X-point. G_{SP} and G_{SI} are the respective control gains for the PI plasma position and shape feedback controllers, G_{XP} and G_{XI} are the PI control gains for the I_p feedback control. G_{SP} and G_{XP} are dimensionless and, G_{SI} and G_{XI} are in s^{-1} .

The coils voltage command values (V_{coil_com}) are calculated considering the mutual interactions between the PF coils an the plasma, the actual values of the PF coil currents, I_p and the mutual inductances. On a real plasma experiment, the mutual inductances between the plasma and the PF coils are unknown due to the difficulty of measuring them directly. Therefore, they are provided by the CCS method. The controller calculates command values of PF coils voltages according to the following equation:

$$V_{com} = G_{vt} \left[M_{coil} \frac{(I_{coil_ref} - I_{coil_meas})}{dt} + \frac{M_{plasma_now} \cdot I_{p_now} - M_{plasma_bfr} \cdot I_{p_bfr}}{dt} \right], \quad (3.4)$$

where M_{coil} represents the mutual inductances between the coils, I_{coil_meas} are the measured coil currents, M_{plasma_now} and M_{plasma_bfr} are the mutual inductances between the plasma and the coils at the current and previous time step, I_{p_now} and I_{p_bfr} are the measured plasma current at the current and previous time step and G_{vt} is the voltage transformer gain.

On the other hand, the in-vessel FPPC coils currents (I_{FPPC_ref}) are calculated with an isoflux control approach which uses proportional-differential (PD) feedback control. In order to reduce the residual between the LCFS flux and two specified control points (Ψ_{SF}) the controller calculates (I_{FPPC_ref}) using:

$$I_{FPPC_ref}(t + \Delta t) = I_{FPPC}(t_0) + M_{FPPC}^\dagger \left[G_{FP}\delta\Psi_{SF}(t) + G_{FD} \frac{d}{dt} \delta\Psi_{SF}(t) \right], \quad (3.5)$$

where M_{FPPC}^\dagger is the 2×2 control matrix which is the pseudo-inverse of the Green function M_{FPPC} , G_{FP} and G_{FD} are the respective PD feedback gains for the plasma position control. G_{FP} is dimensionless and G_{FD} is in s .

3.5 SIMULATION RESULTS

The simulations for the JT60-SA CREATE-NL model, the XSC, the CCS reconstruction method and the QST controller were programmed on top of MATLAB and SIMULINK blocks. This section will address in detail the outcome of the control simulations using a linearized equilibrium given by CREATE-NL for JT60-SA, Scenario 2 at the SOF time frame. The first results to be presented correspond to a gap-based controller using the XSC with different tests cases.

The second part of the results corresponds to isoflux controllers using the XSC with a LCFS reconstruction given by CREATE and also given by the CCS method, as well as the QST controller with the LCFS reconstructed by the CCS method and by CREATE. The figures 3.7 and 3.8 show an overall control block scheme for the simulations. Figure 3.7 corresponds to a configuration using the XSC where the LCFS can be obtained through the CCS method or from the CREATE model. It is worth to point out the existence of the block localized on the bottom part of the scheme called "Vertical Stability Control" along with the XSC. The task of this block is to vertically stabilize the plasma by exploiting the in-vessel coils, which are able to guarantee a faster response due to the fact that the magnetic field generated does not have to penetrate the vessel structures [16]. This controller calculates the voltages at the FPPC coils with the equation:

$$V_{FPPC}(t) = k_1 I_{FPPC}(t) + k_2 \dot{z}_p(t) \quad (3.6)$$

By tuning the gains k_1 and k_2 from equation 3.6 is possible to obtain zero velocity in the vertical plasma direction while maintaining low imbalance current I_{FPPC} in the in-vessel coils [16, Sec. 4.1]. In addition should also be notice the block "Ip Control" which is a Plasma current Controller, which tracks the desired value of the plasma current [27].

Figure 3.8 depicts a configuration using the QST controller receiving as inputs the magnetic fluxes measured at the control points reconstructed either by the CCS method or by the CREATE linearized model.

3.5.1 Disturbances

As far as plasma magnetic control is concerned, the JT60-SA linearized model disturbances have been modeled as variations of β_p and l_i . These disturbances should be in principle rejected by the control systems and maintain in the most accurate possible way the plasma equilibrium. The following set of disturbances have been considered:

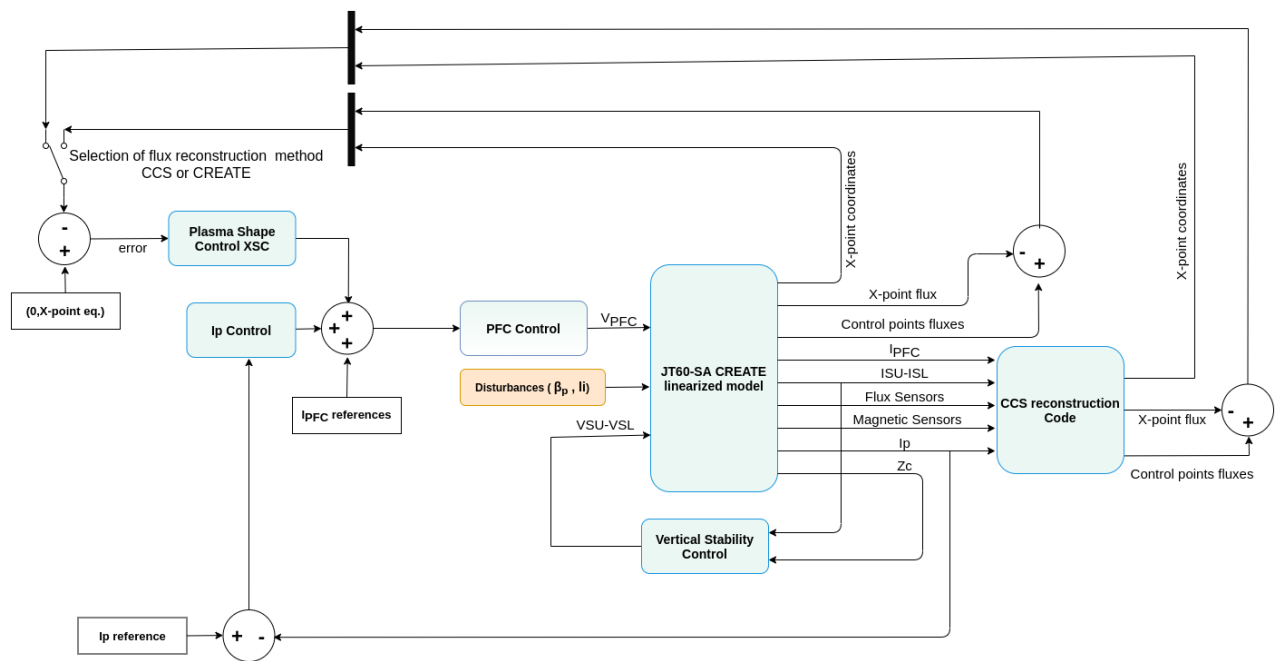


Figure 3.7.: JT-60SA overall control scheme with the CREATE linearized model and the CCS LCFS reconstruction method using the XSC for an isoflux control approach.

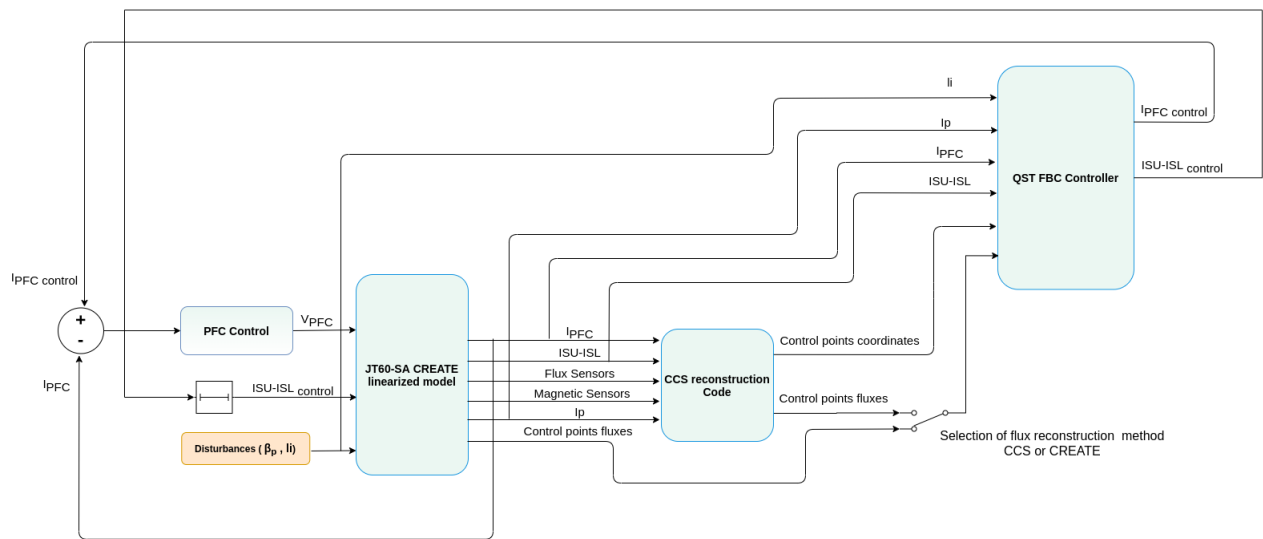


Figure 3.8.: Isoflux control JT-60SA overall scheme with a block for the CREATE JT60-SA linearized model, a block for reconstructing the magnetic fluxes with the CCS method and the QST controller.

- **Disturbance #1** refers to the behavior of β_p and l_i soon after the current flattop is reached, as it was modeled in [28] (in this paper we assume that the flattop is reached at $t \sim 20$ s). As an example, the correspondent time traces are shown in figure 3.9⁴.
- **Disturbance #2** refers to the behaviour of β_p and l_i when a compound ELM⁵ appears during the flattop. As described in [17, p. 34], an instantaneous drop in β_p of $0.05 \beta_{p_{eq}}$ is followed by an exponential recovery with a time constant of 0.05 s with a frequency 10 Hz, l_i is described by an instantaneous drop of 0.06 ($l_{i_{eq}} - 0.5$) followed by an exponential recovery with a time constant of 0.05 s with a frequency 10 Hz. The time traces for β_p and l_i are described in figure 3.10.
- **Disturbance #3** describes an instantaneous drop in l_i of 0.2 ($l_{i_{eq}} - 0.5$) without recovery, simultaneous with a drop on β_p of $0.2 \beta_{p_{eq}}$ followed by a recovery exponential time of 1 s [17, p. 34], which are typical of a so called *minor disruption*. The correspondent time traces for both β_p and l_i are reported in figure 3.11.

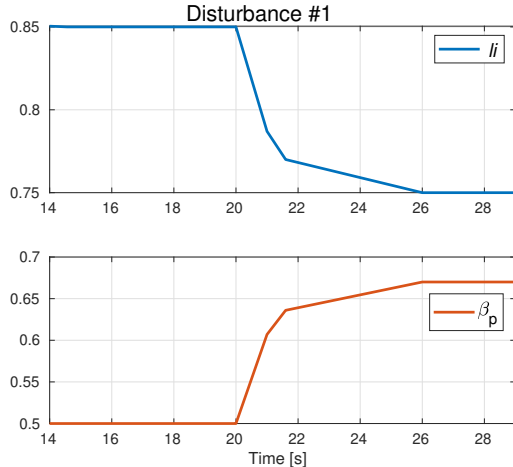


Figure 3.9.: Poloidal beta and internal inductance time traces for Disturbance #1 that models the expected disturbance soon after the plasma current flattop is reached (at $t \sim 20$ s), according to what has been considered in [28].

3.5.2 Gap-based XSC

JT-60SA represents a relevant benchmark to further validate the gap-based control approach, given the high beta regimes that are envisaged during its operation, which represent a challenge from the plasma magnetic control perspective. Different test cases are considered to assess the performance of the proposed shape controller, with the aim of defining an optimal set of gaps to be controlled. This

⁴ The time behavior of both β_p and l_i have been estimated starting from the spatial profiles for both plasma density and temperature envisaged for Scenario 2.

⁵ A compound ELM is commonly referred as multiple clearly distinguishable crash events causing large energy losses [29].

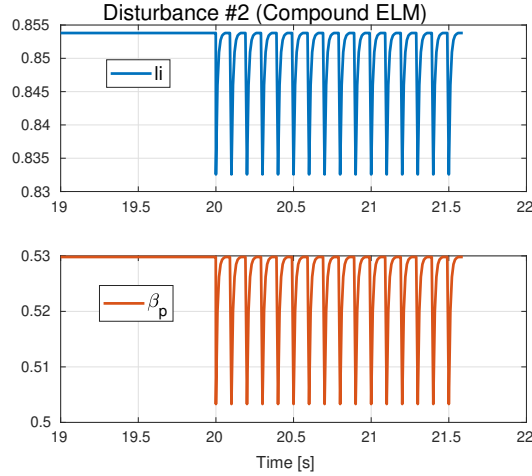


Figure 3.10.: Poloidal beta and internal inductance time traces for Disturbance #2 that models the behavior of these variables due to the presence of a compound ELM as defined in [17].

sections evaluates the steady-state performance of the plasma shape controller under different choices for *gaps* to be controlled.

All around the first wall an equally spaced distribution of 85 gaps was considered as shown in figure 3.5. It should be noticed that all different selections of controlled gaps considered in this paper include the two vertical gaps in the divertor zone, which allows to control the strike-points, and hence the position of the X-point. Other than the whole set of 85 gaps, three additional choices are considered. The first one is reported in figure 3.12a, which consists of 20 gaps equally spaced along the first wall. Moreover, the selection of 8 and 6 gaps that correspond with the control segments considered by the isoflux controllers presented in [30] and [31], respectively, have been also considered (see figures 3.12b and 3.12c). These two latter options are the outcome of preliminary studies aimed at controlling the plasma shape with a set of almost decoupled loops, i.e. SISO, while the XSC approach proposed in this section is intrinsically MIMO. Moreover, it is worth to remark that, although in [30] and [31] the 8 and 6 gap options have been used with an isoflux control approach, here the same control segments have been used to design the XSC adopting a gap-based approach.

The comparison between the various considered gap sets for the different disturbances test cases is summarized in Table 3.1. This table shows the *root-mean-square error* (RMSE) between the reference shape and the shape obtained at steady-state after the occurrence of the disturbances. For all the cases reported in Table 3.1, the RMSE has been computed on the set of 85 gaps shown in figure 3.5, even when not all of them are controlled.

It turns out that, according to this preliminary analysis, the rejection of the disturbances induced by the compound ELMs at steady-state is not an issue at JT-60SA, whatever is the set of gaps that is controlled. Indeed, figure 3.13 shows the RMSE time traces for Disturbance #2 (compound ELMs), being the RMSE computed on the set of 85 gaps shown in figure 3.5 for all the considered options. It turns

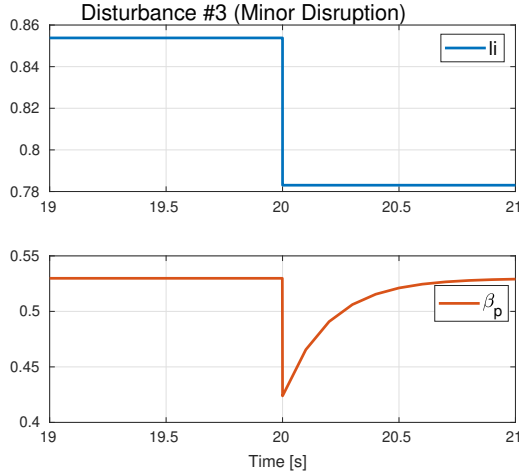


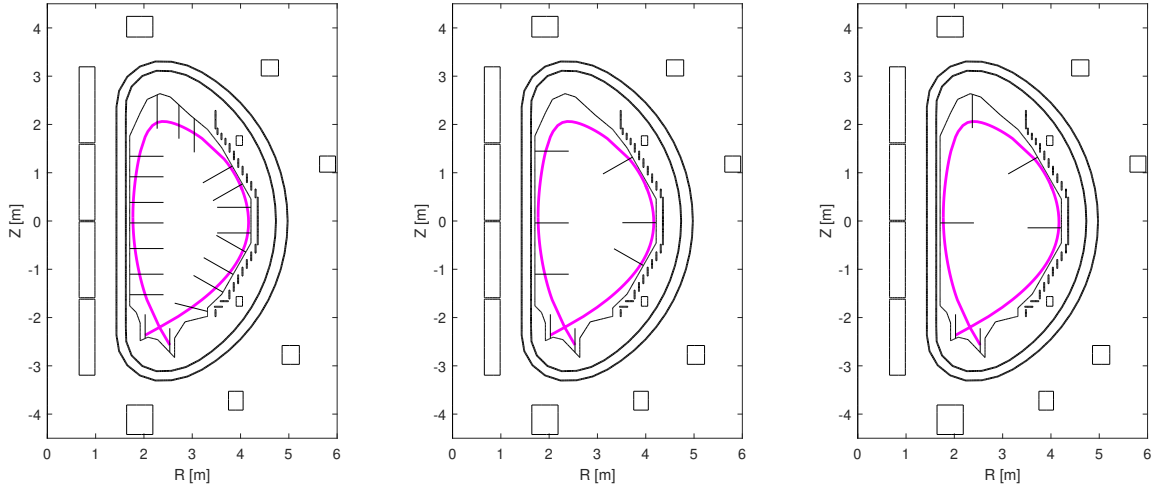
Figure 3.11.: Poloidal beta and internal inductance time traces for Disturbance #3 that models the behavior of these variables due to the presence of a minor disruption as defined in [17].

Steady-state RMSE mm				
	85 gaps	20 gaps	8 gaps	6 gaps
Disturbance #1	7.7	8.7	31.2	19.8
Disturbance # 2 (compound ELM)	~ 0	~ 0	~ 0	~ 0
Disturbance # 3 (Minor disruption)	6.1	7.8	26.9	16.3

Table 3.1.: Steady-state RMSE values for the different choices of number of controlled gaps and for the different disturbances test cases.

out that, whatever gap set is used, the controller has almost the same behavior, with a slightly worse performance of the 6 and 8 gap options. Being a periodic disturbance, the compound ELMs have been applied only during the first part of the simulation, in order to evaluate the steady-state performance of the controller. However, from figure 3.13 it can be noticed that the rejection of the compound ELMs is not a concern even during the transients, being the maximum RMSE ~ 2 mm.

For the other two considered cases, at steady-state, the selection of 85 and 20 gaps have a considerable better RMSE in comparison with the selection of 8 and 6 gaps. As outlined in Table 3.1, the worst case corresponds to the selection of 8 gaps with the presence of Disturbance #3 (minor disruption) during the flattop. As an example, figure 3.15 shows a comparison of the steady-state shape obtained for the 8 and 20 gaps options when the Minor disruption is considered. Figure 3.14 shows the RMSE time traces for this disturbance and it can be noticed that the 20 gaps option gives better results with respect to the 8 and 6 gaps cases also during the transient, and not just in steady-state. In particular, in the 6 and 8 gaps cases, being the number of controlled gaps less than the number of the actuators available for plasma shape control, the steady-state error on the controlled gaps is practically zero. However, not being these two sets of gaps *well representative* of the whole plasma boundary, minimizing the error on such sets does not minimize the error on the whole boundary, as shown in figure 3.14.



(a) The 20 gaps used to assess the performance of plasma shape controller.
 (b) The 8 control segments by the isoflux controller proposed in [30].
 (c) The 6 control segments used by the isoflux controller proposed in [31].

Figure 3.12.: Different choices for the set of controlled gaps used for gap controller.

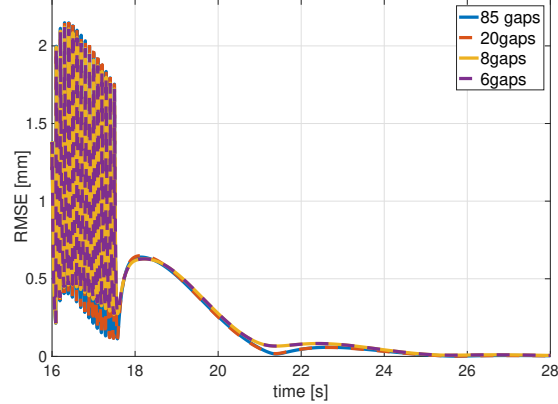


Figure 3.13.: RMSE time traces for the different gaps selections in the presence of Disturbance #2 (compound ELMs). For all the considered cases, the RMSE is computed on the set of 85 gaps shown in figure 3.5.

It should be also noticed that the 6 gaps option considered in [31] gives better performance than the set of 8 gaps chosen in [30]. Indeed, with the latter set, there is a worse control of the plasma top region, as shown in figure 3.15b. Moreover, for the two options with 85 and 20 equally spaced gaps there is no practical difference between the reference shape and the one attained at steady-state. The fact that there is no practical improvement in controlling 85 gaps rather than 20, can be better understood recalling that $\bar{n} < n_{PF}$ singular values are used to compute the control matrix as the pseudo-inverse C^\dagger in (3.1). In particular, only the singular values that are greater than the 5% of the greatest one are used to compute C^\dagger .

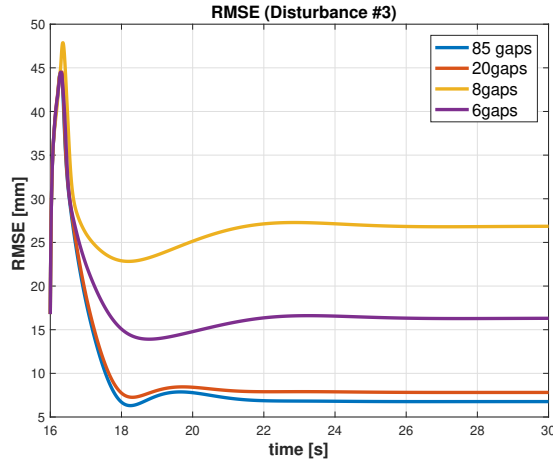


Figure 3.14.: RMSE time traces for the different gaps selections in the presence of Disturbance #3 (minor disruption). For all the considered cases, the RMSE is computed on the set of 85 gaps shown in Fig. 3.5.

3.5.3 Isoflux XSC and QST controller

As mentioned in the previous section, simulations with an isoFlux control approach using the CREATE linearized model and the XSC along with the QST reconstruction and control tools were carried out. The same three disturbances (see figure 3.9, 3.10 and 3.11) and JT60-SA equilibrium scenario from the simulations in last section were used for these test cases for a different number of control points. Due to the vast extension of results, this section will focus on analyze the case for 8 control points in the presence of a Minor disruption with the XSC and the QST controller. Figure 3.16 shows the control points configurations used for carrying out the simulations with an isoFlux shape controller as well as the LCFS's reconstructed by CREATE and the CCS method at steady-state in the presence of a Minor disruption(Disturbance #3).

For the control and reconstruction points configurations a selection of 19 equally spaced descriptors was used (see figure 3.16a), along with the previous 8 and 6 points configurations used for the gap controller. As mentioned before, the CCS method allows a maximum of 19 points for the fluxes reconstruction and the QST controller a maximum of 10 control points, due to these limitations the 19 segments scenario is only feasible using the XSC.

Figure 3.17 compares the steady-state LCFS's for the same disturbance and equilibrium using both controllers, at first glance it is not possible to identify any visible difference between the two controllers, which allows a first conclusion that both controls reject the disturbance and maintain the reference plasma shape in steady-state. For further study in figures 3.18a and 3.18b is presented the behavior of both controllers at the time instant where their fluxes errors are on their highest value, this happens around 2 ms for the case of the XSC and 65 μ s for the QST control after the Minor disruption takes place. From these figures is possible to observe that there is a noticeable plasma shape difference in

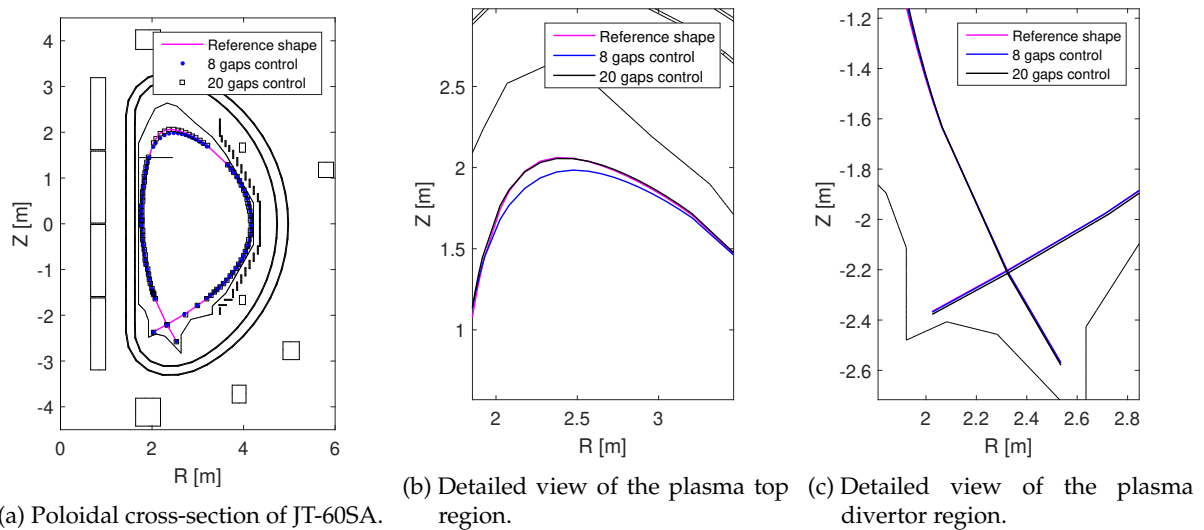


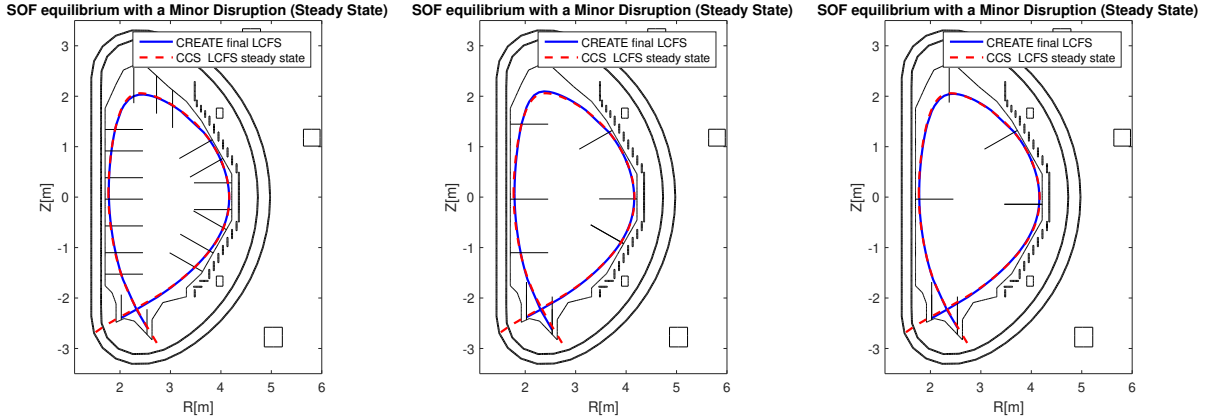
Figure 3.15.: Comparison of the shape controller performance in the presence of Disturbance #3 (minor disruption). The two cases of 8 and 20 gaps are considered.

comparison with the one from the equilibrium, specially on the radial outer region and secondly is visible that the difference between the equilibrium and the steady-state shape is smaller for the QST controller case.

Figure 3.19 shows the time traces comparing the flux at the X-point and the 8 control points fluxes, for the XSC and the QST control cases. From these two graphs is noticeable that the QST controller takes around 0.5 s more to reach the steady-state after the disturbance takes place than XSC , but the fluxes at the control points reach a state-state flux value way closer to the X-point flux than the fluxes using the XSC for the simulation, in addition figure 3.20 shows the flux error time traces on the 8 control points for both controllers, on these plots is worth to mention that additionally to a smaller state-state error using the QST control, the maximum error values which are located right after the disturbance takes place are higher for the simulation using the XSC.

In order to summarize all the results from the tested cases, tables 3.3 , 3.5 and 3.7 outline the control points fluxes RMSE and tables 3.3, 3.5 and 3.7 present the X-point radial and vertical position errors in steady-state, these tables summarize results for all the different number of control points with the three different disturbances. Some of the main aspects that are possible to conclude from the tables results are :

- (a) For all disturbances the 8 control points selection has the biggest fluxes and X-point position steady-state errors and the cases with 19 control points the lesser ones.
- (b) Disturbance #2 (Compound ELM) results present the lesser flux RMSE values in comparison with the other two disturbances. See table 3.4.
- (c) The simulations using the QST controller present practically a flux RMSE equal to zero in steady-state for all disturbances while the XSC does not.



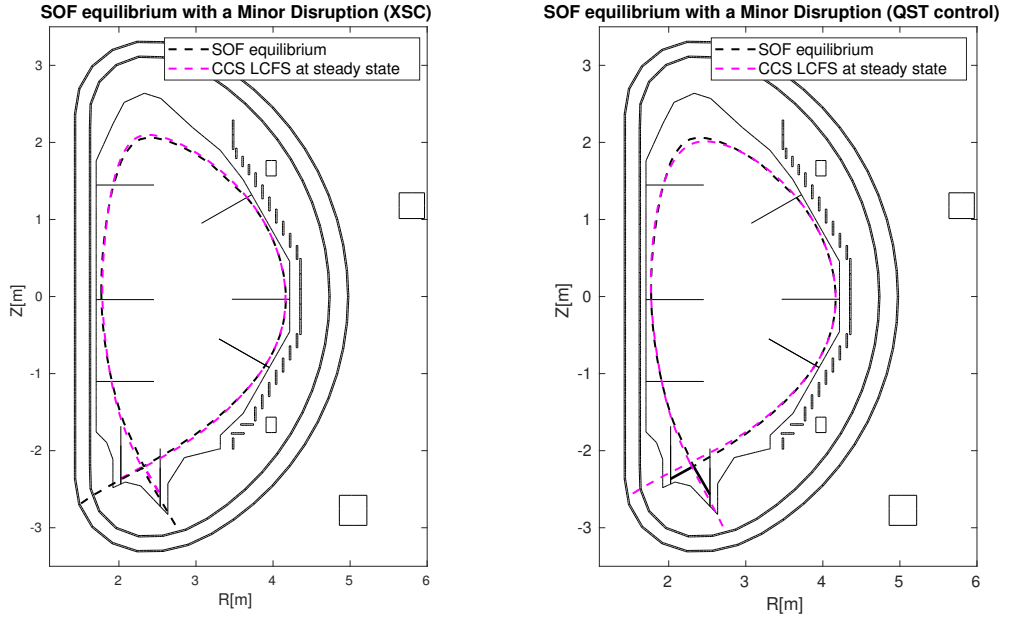
- (a) The 19 control segments used to assess the performance of plasma shape controller.
- (b) The 8 control segments by the isoflux controller proposed in [30].
- (c) The 6 control segments used by the isoflux controller proposed in [31].

Figure 3.16.: LCFS reconstructed by CREATE and the CCS code for the JT60-SA scenario 2 SOF equilibrium with a Minor disruption at steady-state for the three considered selection of control segments using the XSC with an isoflux approach.

Controller	eXtreme Shape Controller	QST Controller	
LCFS reconstruction method	CCS	CREATE	CCS
6 points	0.0116	0.0133	~ 0
8 points	0.0166	0.0181	~ 0
19 points	0.0085	0.0088	

Table 3.2.: Steady-state flux RMSE values for the different selection of control points for the JT60-SA scenario 2, SOF equilibrium in the presence of Disturbance #1 at $t \sim 20$ s.

- (d) For all the scenarios the vertical XSC X-point error is at least %30 greater than the radial position error, while for the QST control the vertical position error tends to be around %50 lesser than the radial position.
- (e) As mentioned on the previous section and as it can be observe on the scheme in figure 3.7, the XSC isoflux approach also controls the X-point position, this is noticeable for all the disturbances with 8 control points, where the vertical and horizontal position error values with the QST controller are at least 50% greater than the ones with the XSC .
- (f) Despite the X-point control dynamics embedded on the XSC, for the 6 control points scenarios, the radial X-point error positions are similar between the XSC and the QST control simulations, and the vertical X-point error using the XSC is for all disturbances at least 10 times greater than the simulations with the QST controller.



(a) Comparison between the reference shape (i.e., the shape at the considered equilibrium) and the LCFS reconstructed by the CCS code at steady-state in the presence of the minor disruption using the XSC for the plasma shape, when 8 control segments are considered.

(b) Comparison between the reference shape (i.e., the shape at the considered equilibrium) and the LCFS reconstructed by the CCS code at steady-state in the presence of a minor disruption using the QST controller for the plasma shape and current and 8 control segments .

Figure 3.17.: CREATE-NL JT60-SA Scenario 2 - SOF equilibrium compared with the LCFS reconstructed by the CCS method for 8 control points in the presence of a Minor disruption at steady-state using both the XSC and the QST control.

3.5.4 Shape reference change

A change in the plasma shape for the Scenario 2 - SOF equilibrium has been also considered. In this test scenario closed-loop simulations with the CCS reconstruction method and the isoflux XSC for the plasma shape were performed. Since the configuration with 8 control points seems to be for all cases the one most challenging due to the error values in steady-state obtained on the past subsection, these selection of control points was used for this simulation. The transition time from the initial shape to the target was set equal to 1.5 s. Figure 3.21 shows the equilibrium LCFS (Scenario 2 -SOF), the desired target shape and the LCFS at steady state reconstructed by the CCS method. It can be noticed that the controller is able to track the required shape with negligible error at steady-state, taking ~ 6 s to reach to it. Figure 3.22 shows the time traces for the fluxes at the 8 control points compared with the X-point flux and figure 3.23 shows the correspondent control flux errors.

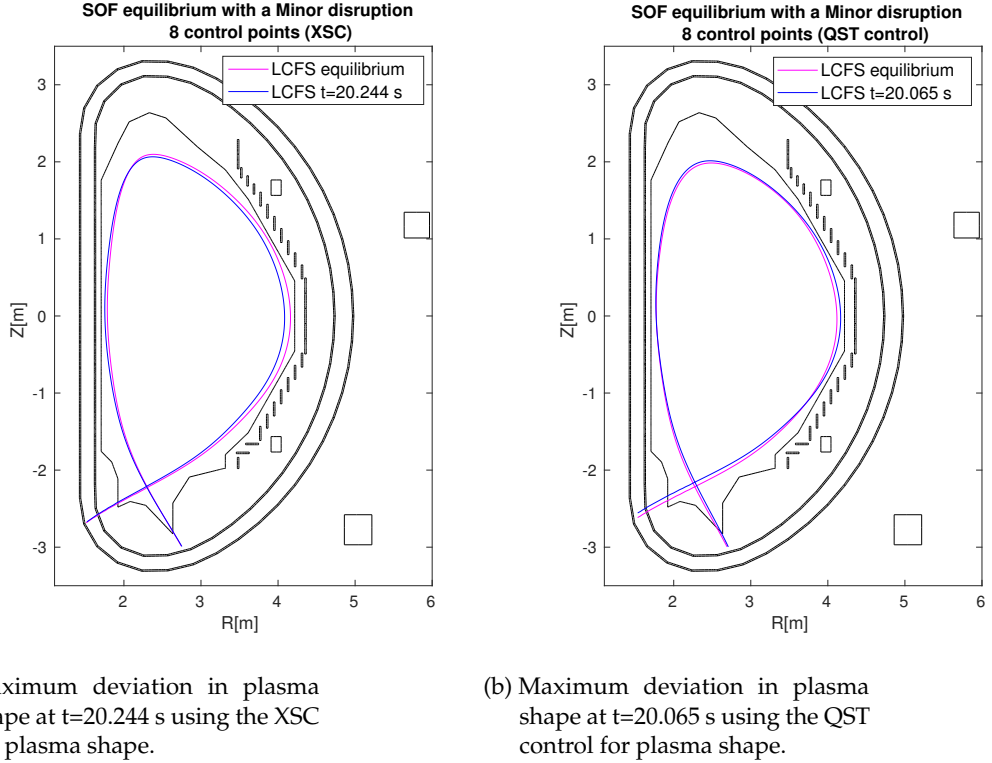


Figure 3.18.: CREATE-NL JT60-SA Scenario 2 - SOF equilibrium compared with the LCFS reconstructed by the CCS method for 8 control points in the presence of a Minor disruption (Disturbance #3) at the time of maximum deviation for both cases. As shown in figure 3.11, the disturbance occurs at $t \sim 20$ s

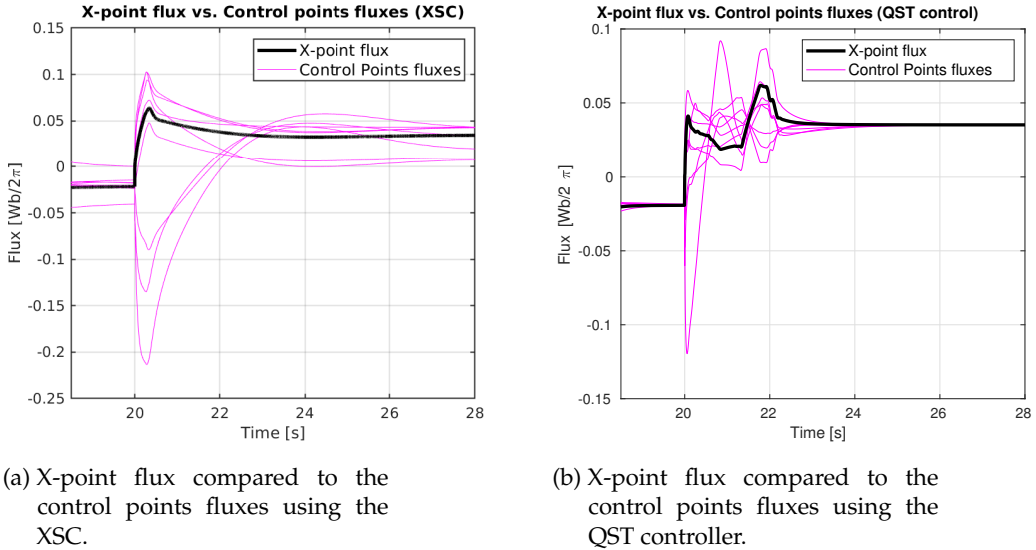
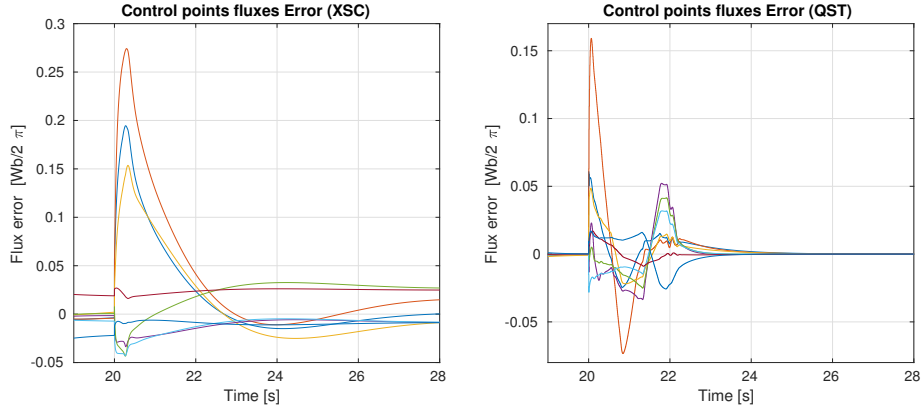


Figure 3.19.: Comparison between the flux at the X-point and the fluxes in the 8 control points reconstructed by the CCS method, when a Minor disruption is applied at $t=20$ s using the XSC and the QST controller. It should be noticed that QST control has a faster performance to reach the steady-state and less error.



(a) Flux errors using the XSC for 8 control points in the presence of a Minor disruption starting at $t = 20$.

(b) Flux errors using the QST controller for 8 control points in the presence of a Minor disruption starting at $t = 20$.

Figure 3.20.: Flux errors for the case of 8 control points in the presence of a Minor disruption using the XSC and the QST controller. Even though both controllers reject the disturbance, it is possible to remark how the QST control has an overall smaller error.

Disturbance #1 steady state X-point position error								
Controller	eXtreme Shape Controller				QST Controller			
LCFS reconstruction method	CCS		CREATE		CCS		CREATE	
	Rx mm	Zx mm	Rx mm	Zx mm	Rx mm	Zx mm	Rx mm	Zx mm
6 points	-4.606	19.96	-3.576	28.16	-1.434	-0.843	-1.16	-0.316
8 points	18.58	21.95	18.96	29.82	49.16	-46.52	59.66	-40.92
19 points	2.62	12.84	2.375	20.51				

Table 3.3.: X-point position steady state error for JT60-SA scenario 2, SOF equilibrium in the presence of Disturbance #1 at $t \sim 20$ s. The XSC and QST controller were used in different simulations for the shape control along with two reconstruction methods for the LCFS.

Disturbance #2 (Compound ELM) flux RMSE steady state $\text{Wb}/2\pi$			
Controller	eXtreme Shape Controller		QST Controller
LCFS reconstruction method	CCS	CREATE	CCS
6 points	0.0014	0.0022	~ 0
8 points	0.0104	0.0101	~ 0
19 points	0.0023	0.0028	~ 0

Table 3.4.: Steady-state flux RMSE values for the different selection of control points for the JT60-SA scenario 2, SOF equilibrium in the presence of Disturbance #2 (Compound ELM) at $t \sim 20$ s.

Disturbance #2 (Compound ELM) steady state X-point position error								
Controller	eXtreme Shape Controller				QST Controller			
LCFS reconstruction method	CCS		CREATE		CCS		CREATE	
	Rx mm	Zx mm	Rx mm	Zx mm	Rx mm	Zx mm	Rx mm	Zx mm
6 points	0.3968	-2.455	1.3	2.556	-0.481	-0.267	-0.019	0.0143
8 points	15.72	-8.41	16.61	-3.098	50.18	-43.25	54.44	-32.68
19 points	-0.0007	0.0237	-0.1916	-4.69				

Table 3.5.: X-point position steady state error for JT60-SA scenario 2, SOF equilibrium in the presence of Disturbance #2 (Compound ELM) at $t \sim 20$ s. The XSC and QST controller were used in different simulations for the shape control along with two reconstruction methods for the LCFS.

Disturbance #3 (Minor disruption) flux RMSE steady state Wb/2π			
Controller	eXtreme Shape Controller		QST Controller
LCFS reconstruction method	CCS	CREATE	CCS
6 points	0.0121	0.0139	~ 0
8 points	0.0152	0.0170	~ 0
19 points	0.0069	0.0088	

Table 3.6.: Steady-state flux RMSE values for the different selection of control points for the JT60-SA scenario 2, SOF equilibrium in the presence of Disturbance #3 (Minor disruption) at $t \sim 20$ s.

Disturbance #3 (Minor disruption) steady state X-point position error								
Controller	eXtreme Shape Controller				QST Controller			
LCFS reconstruction method	CCS		CREATE		CCS		CREATE	
	Rx mm	Zx mm	Rx mm	Zx mm	Rx mm	Zx mm	Rx mm	Zx mm
6 points	-4.92	20.9	-3.57	28.8	-2.70	-0.105	-2.24	0.369
8 points	17.44	21.56	17.81	29.04	47.08	-46.56	57.61	-41.42
19 points	-5.54	16.78	-4.42	24.41				

Table 3.7.: X-point position steady state error for JT60-SA scenario 2, SOF equilibrium in the presence of Disturbance #3 (Minor disruption) at $t \sim 20$ s. The XSC and QST controller were used in different simulations for the shape control along with two reconstruction methods for the LCFS.

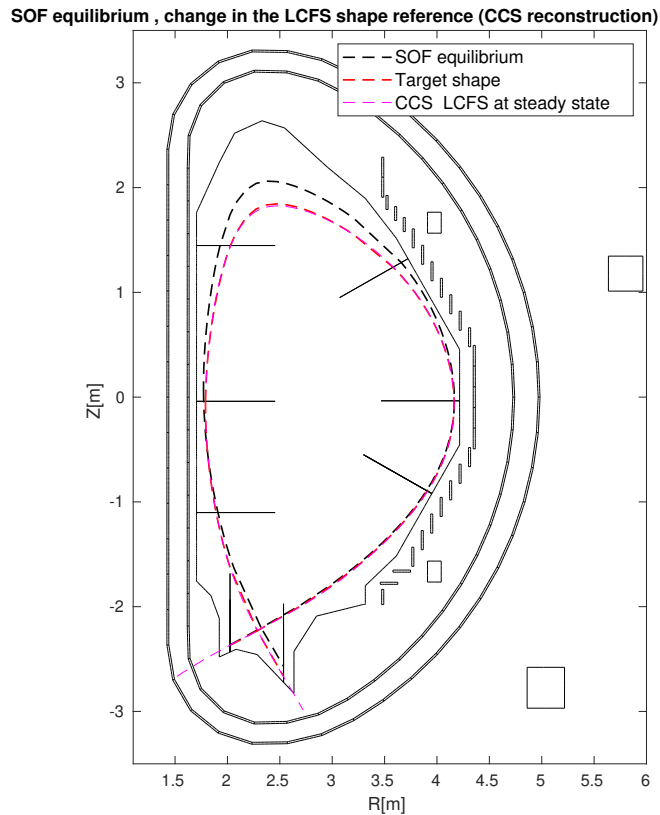


Figure 3.21.: XSC isoflux response to a change of shape request. The dashed black shape is the starting shape, while the red one is the target shape. The magenta dashed shape is the LCFS at steady state.

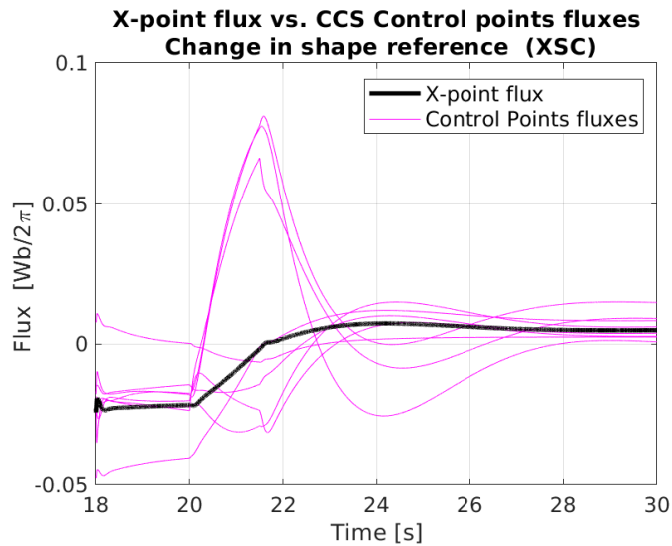


Figure 3.22.: Comparison between the flux at the X-point and the fluxes a

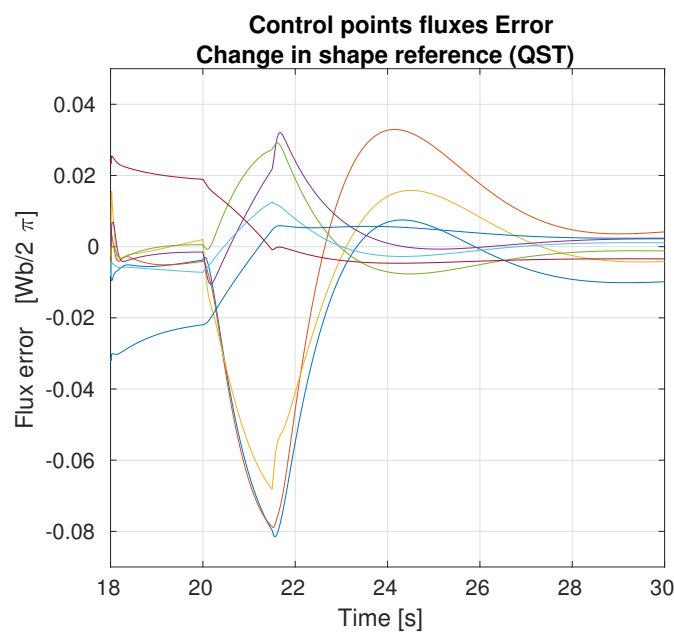


Figure 3.23.: Flux control error for the case of 8 control points for a change in the shape reference between 20 and 21.5 s.

4

ISTTOK

4.1 MACHINE DESCRIPTION

4.2 DIAGNOSTICS AND ACTUATORS

4.3 ATCA-MIMO-ISOL BOARDS

4.3.1 *Hardware layout*

4.3.2 *Real-time integration software*

4.4 PLASMA CURRENT MAGNETIC FIELD

Retrieving the contribution of the plasma current in tokamaks ...

The methods of correction of the magnetic error fields due to inaccuracies of tokamak manufacturing and assembly are considered. The problems of the plasma position and shape reconstruction based on magnetic field measurements are discussed.

4.5 PLASMA CENTROID POSITION DETERMINATION

5

ISTTOK RESULTS

This chapter describes the latest implementations in ISTTOK MARTe framework followed by the presentation of the obtained results for control of the current centroid position.

5.1 IMPLEMENTATION OF THE GENERAL APPLICATION MODULES

General Application Modules (GAM)

5.1.1 *PID control implementation*

Proportional-Integrative-Derivative

5.1.2 *Data-driven state-space model retrieving*

Early efforts in finding a real-time equilibrium solver for ISTTOK were performed in the last years. Due to the geometrical conditions it was never retrieve a

5.1.3 *Kalman filter implementation*

5.1.4 *Multiple-Input Multiple-Output control implementation*

5.2 PLASMA CURRUENT CENTROID POSITION CONTROL RESULTS

This section addresses the latest results from the real-time implementation of control algorithms in ISTTOK.

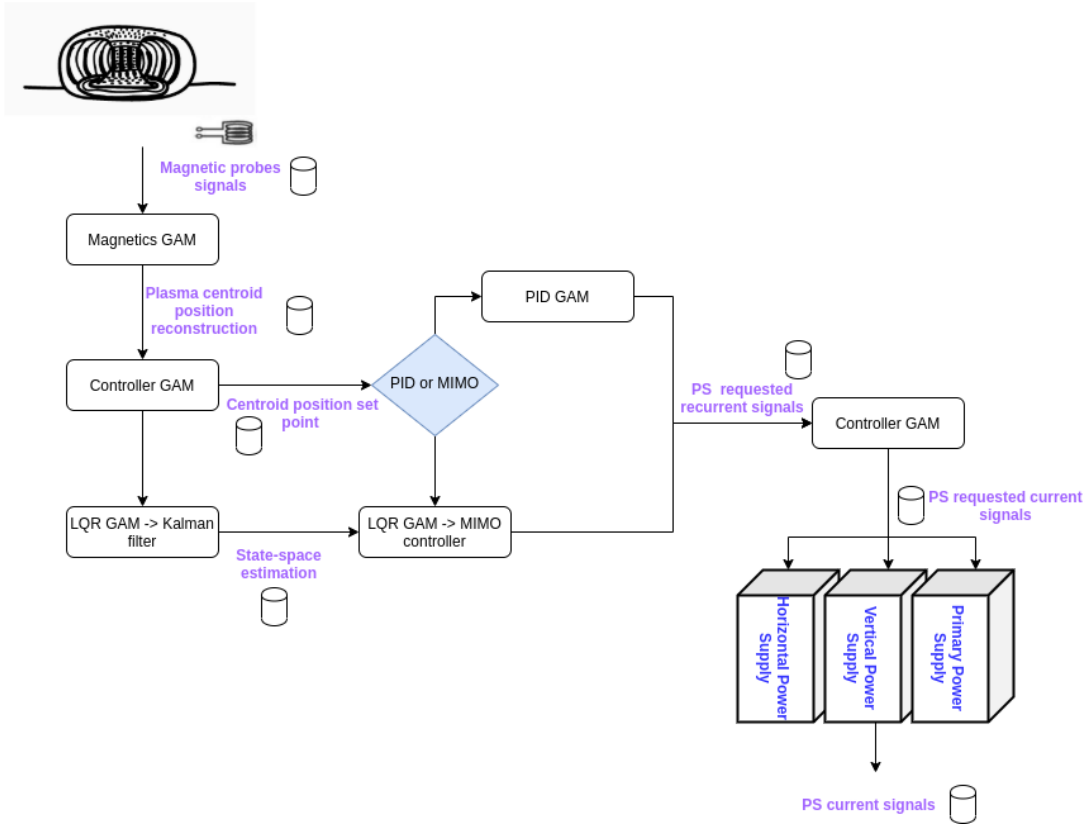


Figure 5.1.: ISTTOK MARTe overall control position scheme

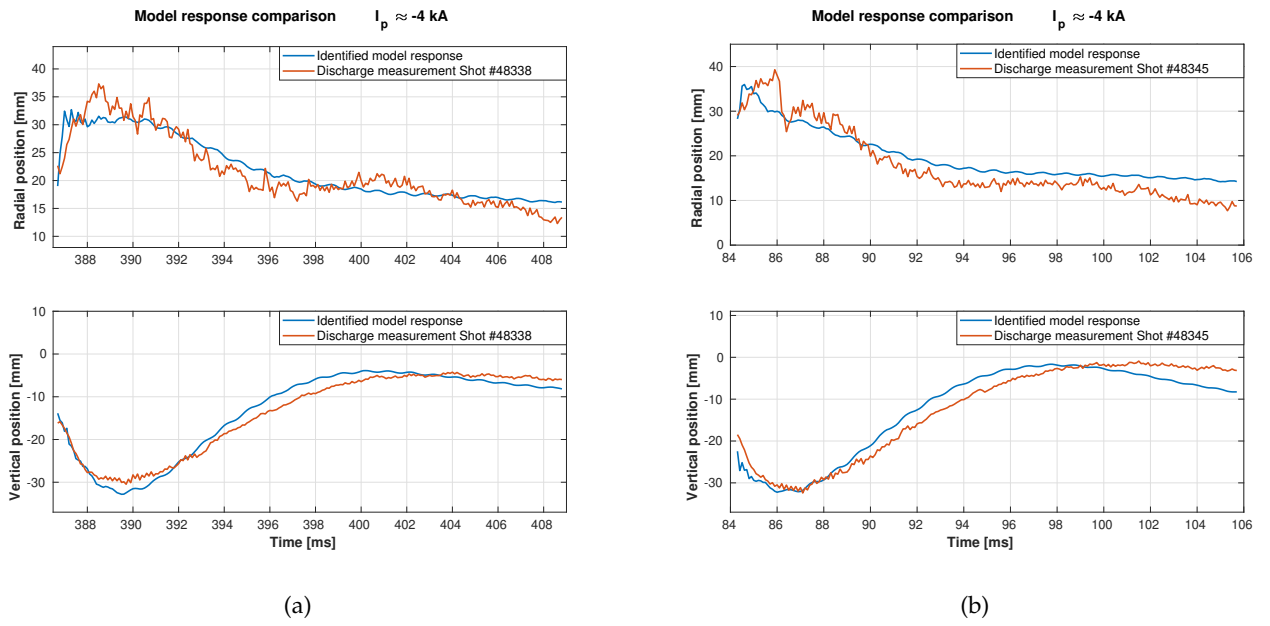


Figure 5.2.: Fig.

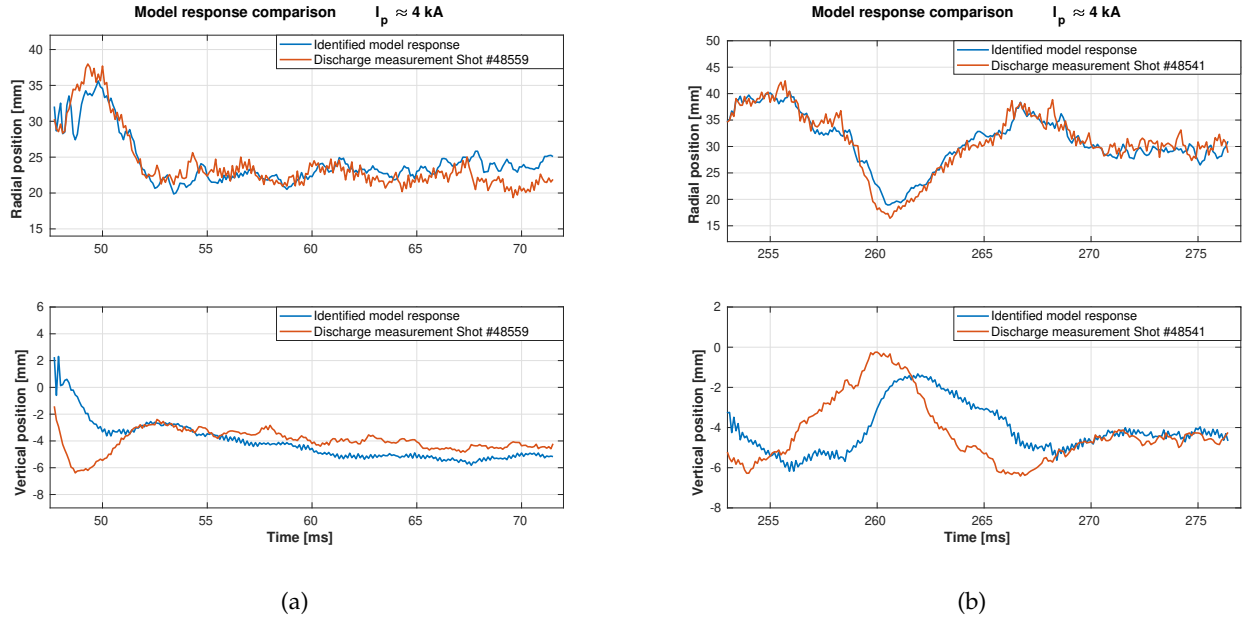
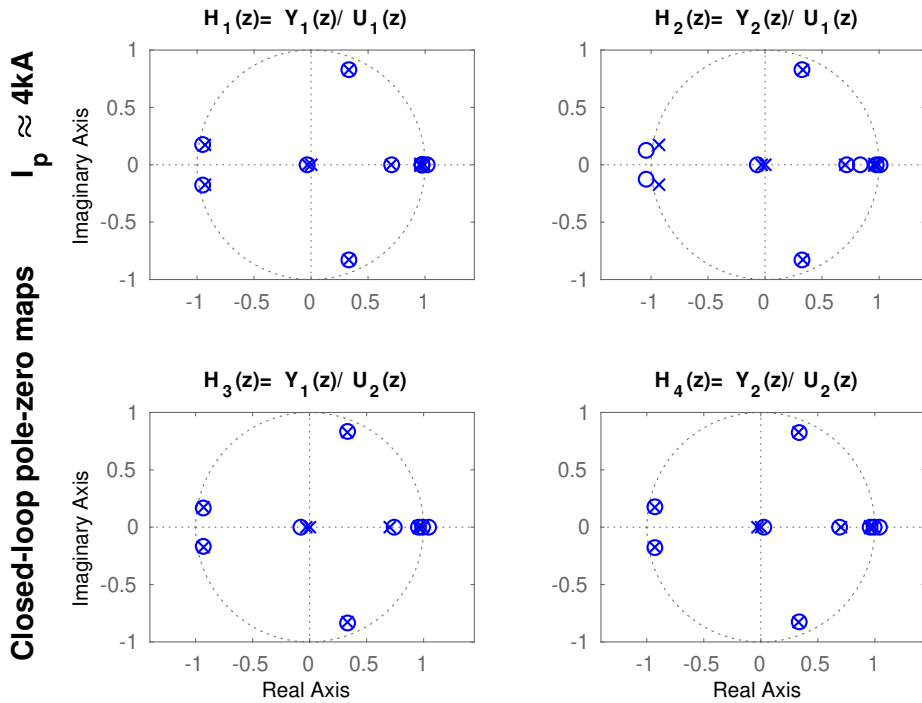
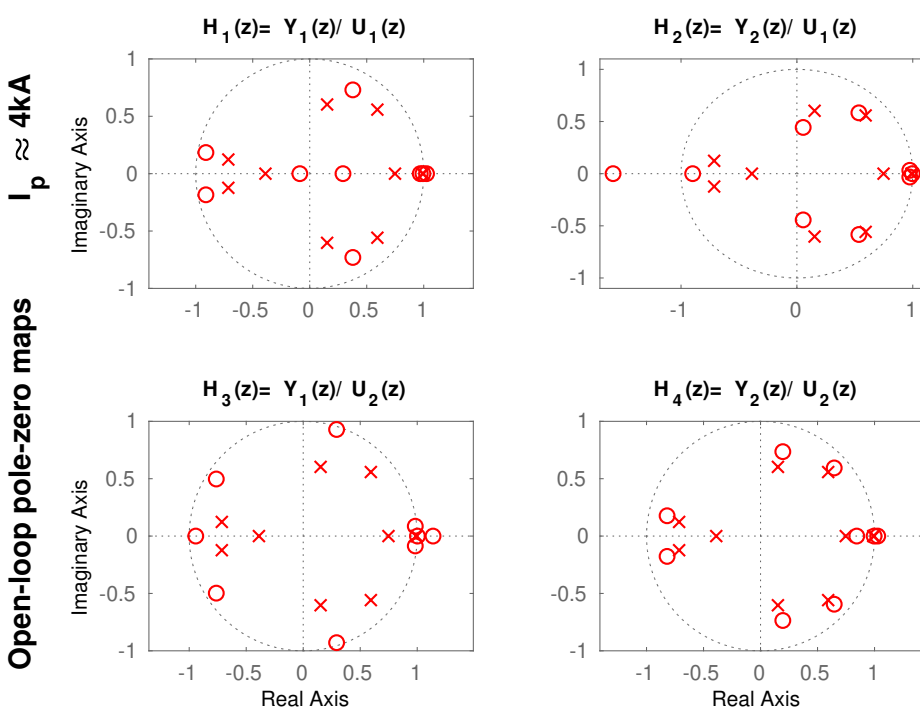
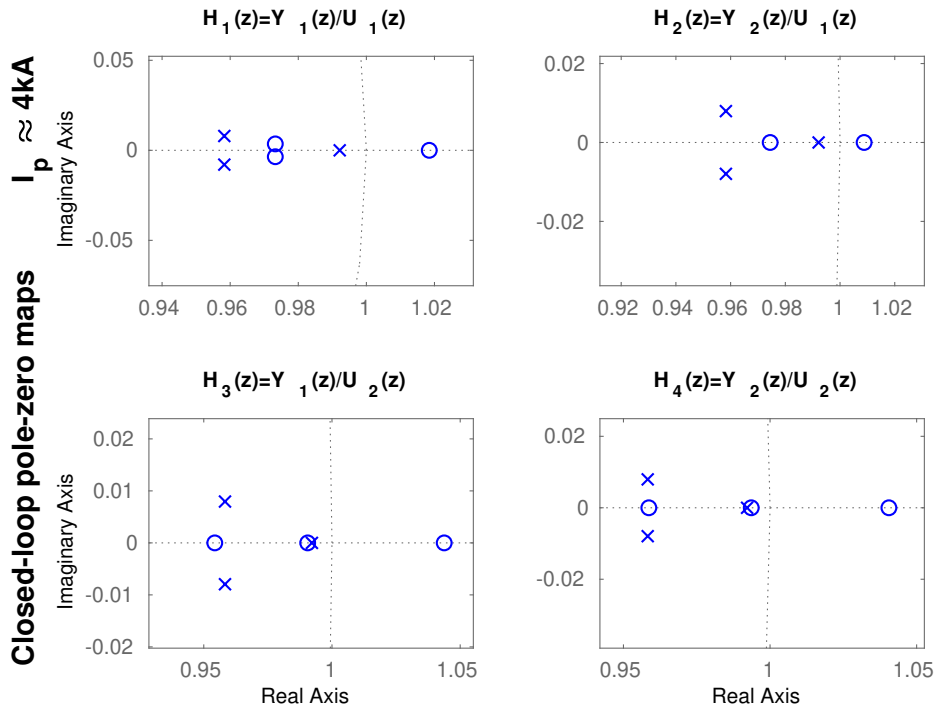
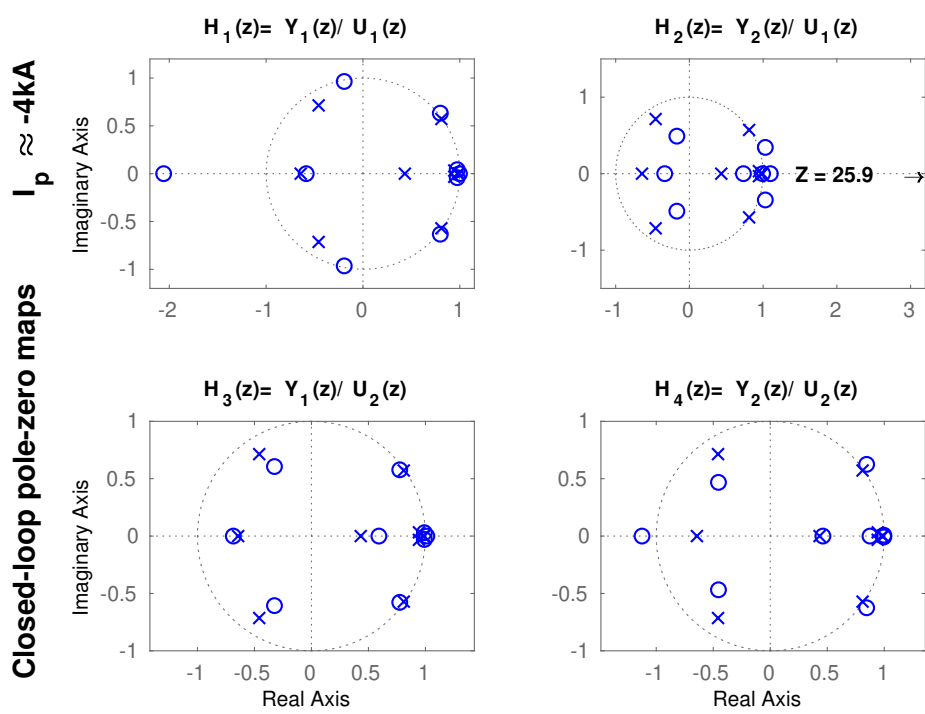
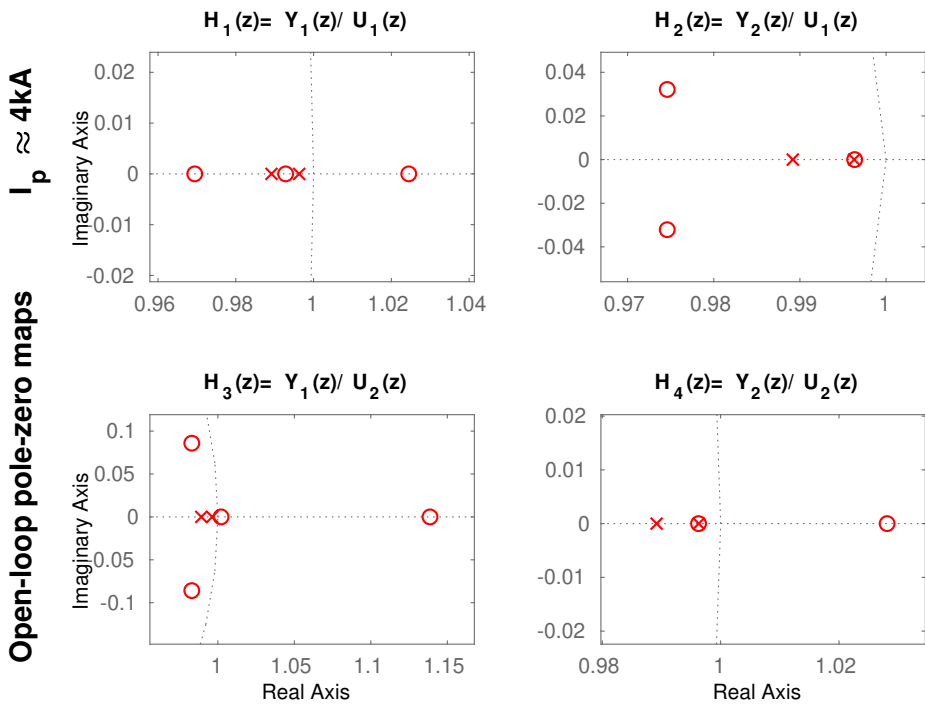
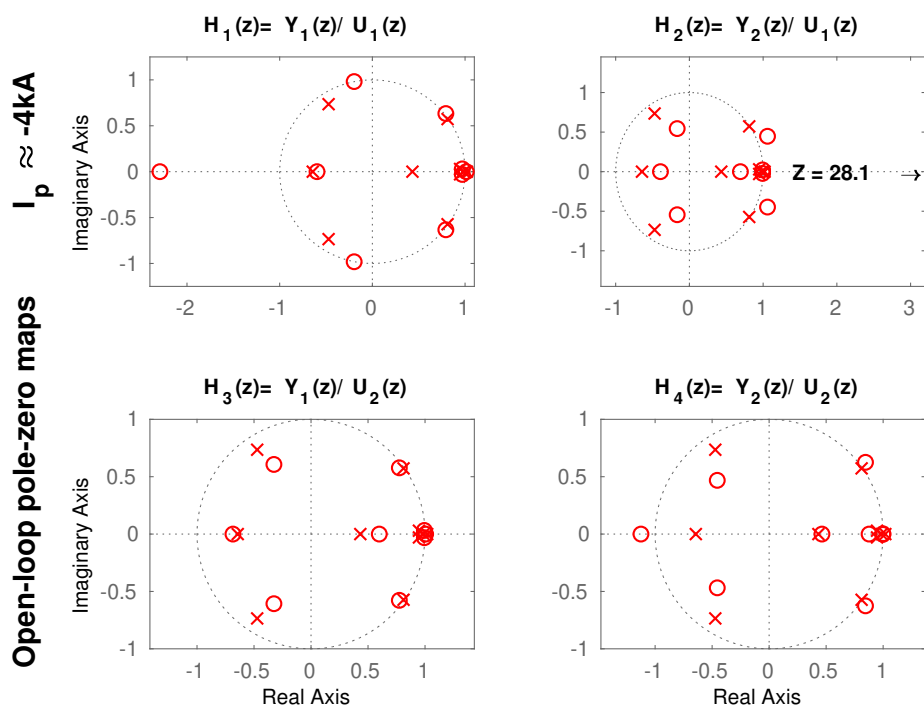
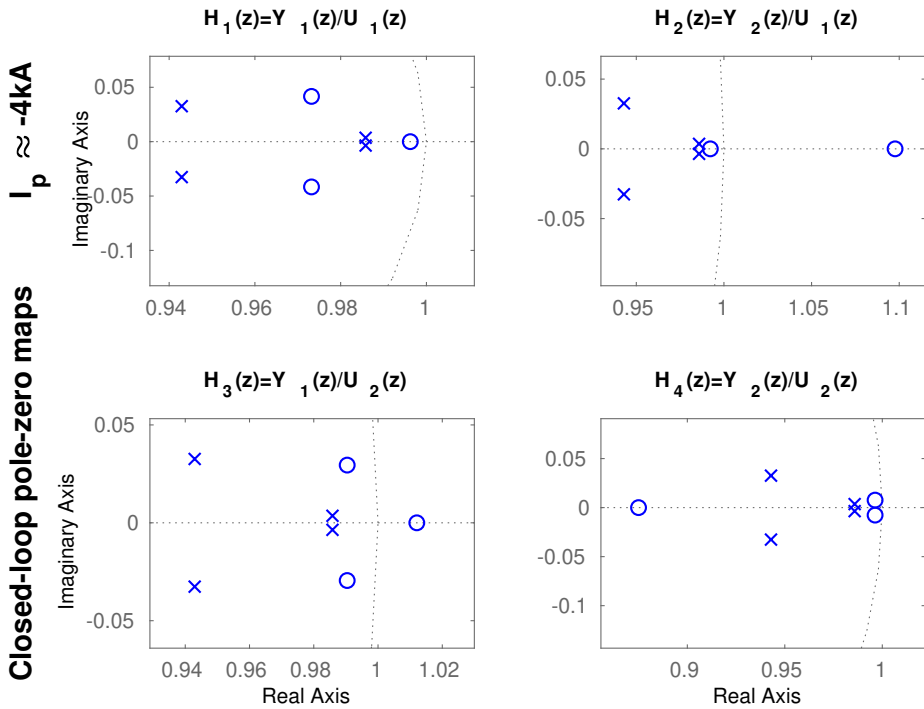


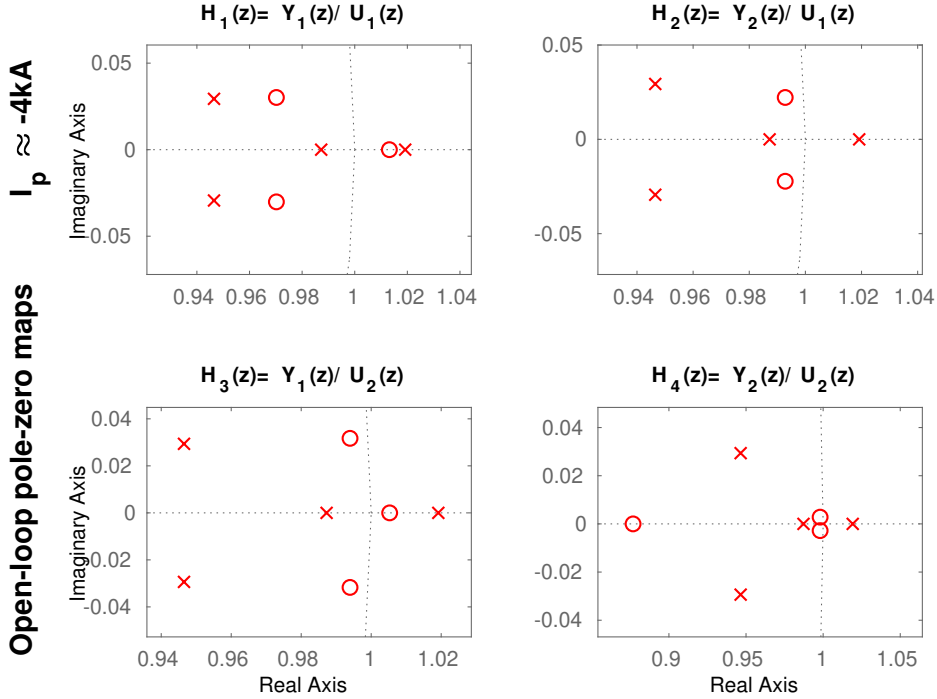
Figure 5.3.: Fig.


 Figure 5.4.: Pole-Zero maps in closed loop for the model when $I_p \approx 4\text{kA}$. Superposition of poles and zeros can be seen in the four transfer functions.









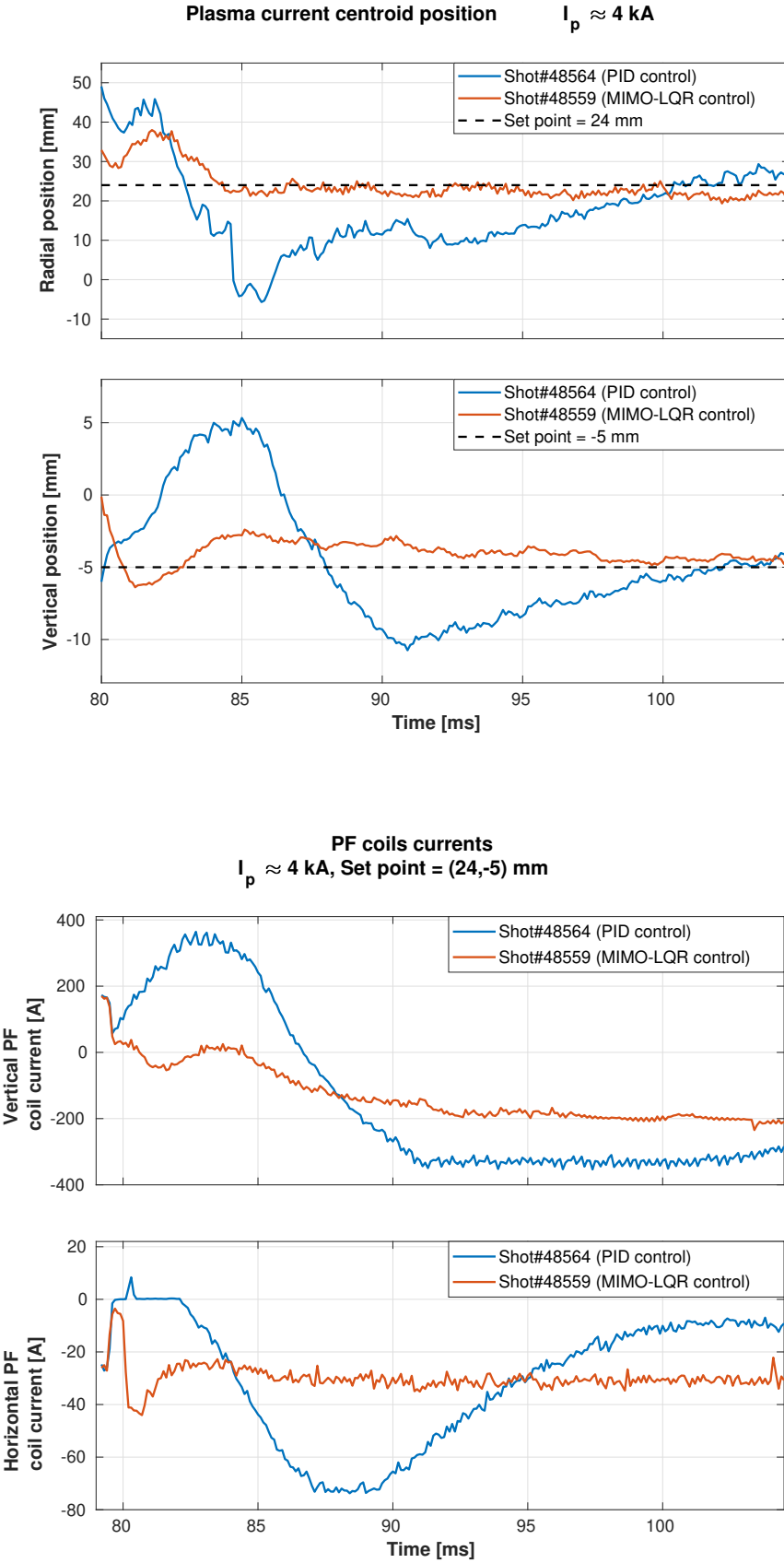
5.2.1 PID control and LQR control results

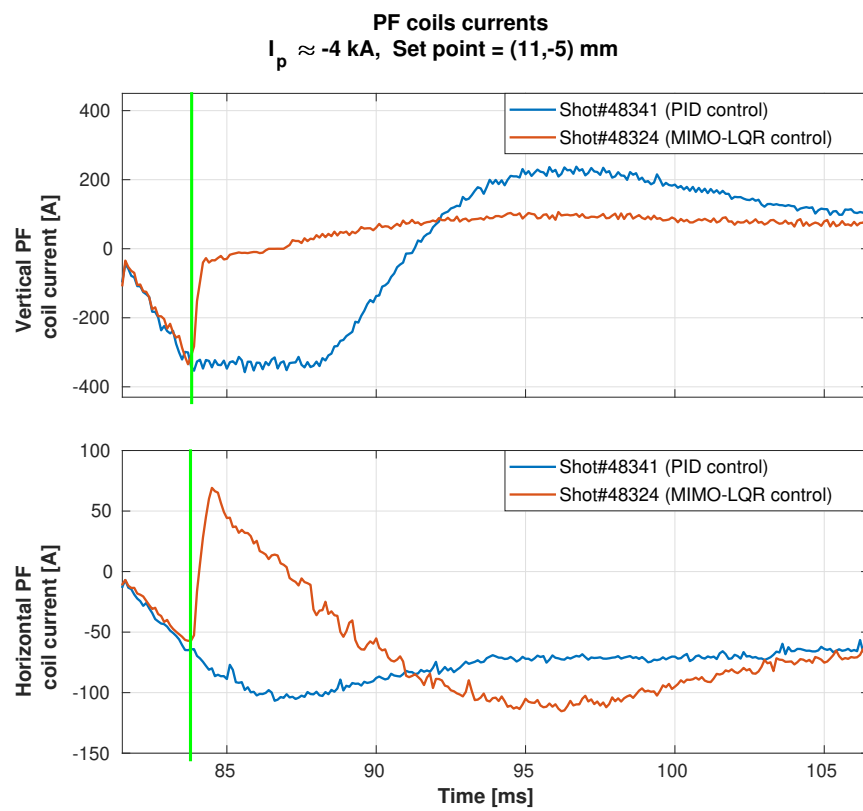
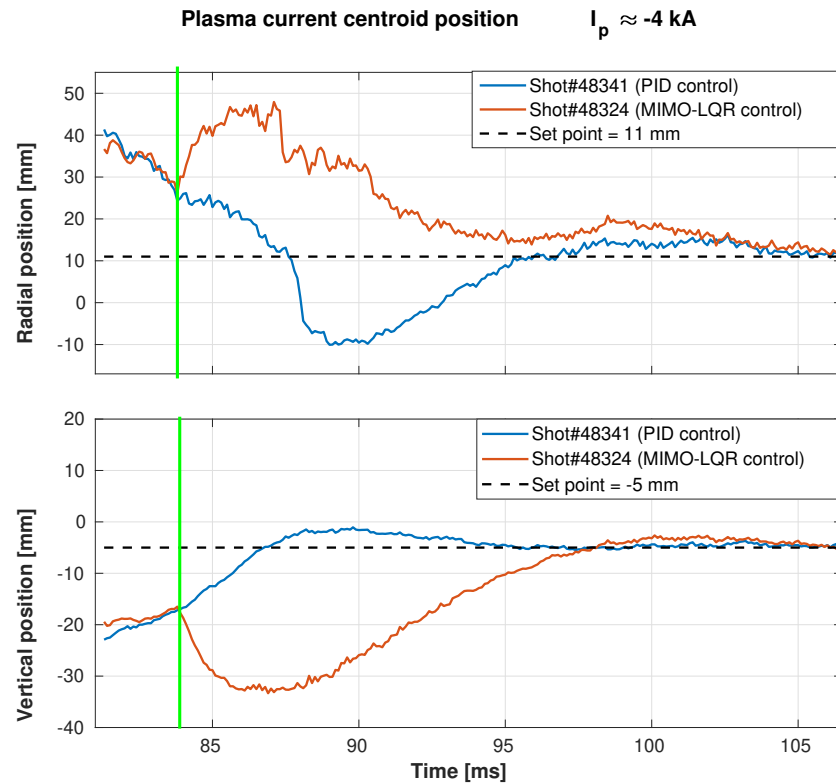
This section addresses obtained the experimental results in ISTTOK's plasma discharges.

Control	Shot #	RMSE (R, z) mm	Set point (R, z) mm	I_p
PID	48564	(13.73, 4.4102)	(24, -5)	$\approx 4kA$
MIMO LQR	48559	(4.2252, 1.4215)	(24, -5)	$\approx 4kA$
PID	48563	(13.6717, 4.1652)	(24, -4)	$\approx 4kA$
MIMO LQR	48561	(8.1047, 3.2752)	(24, -4)	$\approx 4kA$
PID	48556	(12.0315, 3.3217)	(32, -5)	$\approx 4kA$
MIMO LQR	48555	(4.2618, 2.4698)	(32, -5)	$\approx 4kA$
PID	48551	(13.9998, 3.3431)	(27, -5)	$\approx 4kA$
MIMO LQR	48554	(5.9830, 2.0062)	(27, -5)	$\approx 4kA$
PID	48515	(6.0178, 2.6123)	(30, -5)	$\approx 4kA$
MIMO LQR	48541	(5.8372, 1.7664)	(30, -5)	$\approx 4kA$
PID	48544	(4.8745, 2.5167)	(32, -4)	$\approx 4kA$
MIMO LQR	48542	(4.4346, 3.6573)	(32, -4)	$\approx 4kA$
PID	48546	(11.4560, 3.4765)	(27, -7)	$\approx 4kA$
MIMO LQR	48548	(7.6745, 4.1569)	(27, -7)	$\approx 4kA$
PID	48341	(12.0959, 5.7652)	(11, -5)	$\approx -4kA$

MIMO LQR	48324	(15.4768, 14.3436)	(11, -5)	$\approx -4kA$
PID	48340	(11.7701, 5.9599)	(11.2, -5.5)	$\approx -4kA$
MIMO LQR	48338	(11.5260, 12.6226)	(11.2, -5.5)	$\approx -4kA$
PID	48343	(15.7675, 5.7453)	(12, -5)	$\approx -4kA$
MIMO LQR	48342	(14.5168, 14.4329)	(12, -5)	$\approx -4kA$
PID	48346	(12.4228, 6.1541)	(12.2, -5.3)	$\approx -4kA$
MIMO LQR	48345	(9.7513, 13.0338)	(12.2, -5.3)	$\approx -4kA$
PID	48349	(19.3397, 5.5406)	(11.5, -5.6)	$\approx -4kA$
MIMO LQR	48348	(9.1727, 13.1505)	(11.5, -5.6)	$\approx -4kA$
PID	48352	(15.2181, 6.5395)	(10.8, -4.7)	$\approx -4kA$
MIMO LQR	48354	(14.6405, 13.7307)	(10.8, -4.7)	$\approx -4kA$
PID	48351	(13.4078, 5.8769)	(13.2, -5.6)	$\approx -4kA$
MIMO LQR	48350	(13.9320, 14.4940)	(13.2, -5.6)	$\approx -4kA$

Table 5.1.: Centroid position RMSE comparison between PID and MIMO-LQR controlled discharges for different set points and plasma current scenarios.





6

CONCLUSIONS

bla bla bla

BIBLIOGRAPHY

- [1] Andrej A. Kavin Valerij A. Belyakov. *Fundamentals of Magnetic Thermonuclear Reactor Design*. Elsevier, 2018.
- [2] J. R. Ferron, A. Kellman, E. McKee, T. Osborne, P. Petrach, T. S. Taylor, J. Wight, and E. Lazarus. An advanced plasma control system for the dIII-d tokamak. In [*Proceedings*] *The 14th IEEE/NPSS Symposium Fusion Engineering*, pages 761–764 vol.2, Sep. 1991.
- [3] B. G. Penaflor, J. R. Ferron, A. W. Hyatt, M. L. Walker, R. D. Johnson, D. A. Piglowski, E. Kolemen, A. S. Welander, and M. J. Lanctot. Latest advancements in DIII-D Plasma Control software and hardware. *2013 IEEE 25th Symposium on Fusion Engineering, SOFE 2013*, pages 1–4, 2013.
- [4] M. Margo, B. Penaflor, H. Shen, J. Ferron, D. Piglowski, P. Nguyen, J. Rauch, M. Clement, A. Battey, and C. Rea. Current State of DIII-D Plasma Control System. *Fusion Engineering and Design*, 150(October 2019), 2020.
- [5] Mellanox Technologies. Introduction to InfiniBand. Technical report, 2003.
- [6] J. I. Paley, S. Coda, B. Duval, F. Felici, and J. M. Moret. Architecture and commissioning of the TCV distributed feedback control system. *Conference Record - 2010 17th IEEE-NPSS Real Time Conference, RT10*, pages 1–6, 2010.
- [7] H. Anand, C. Galperti, S. Coda, B. P. Duval, F. Felici, T. Blanken, E. Maljaars, J. M. Moret, O. Sauter, T. P. Goodman, and D. Kim. Distributed digital real-time control system for the TCV tokamak and its applications. *Nuclear Fusion*, 57(5), 2017.
- [8] A. C. Neto, F. Sartori, F. Piccolo, R. Vitelli, G. De Tommasi, L. Zabeo, A. Barbalace, H. Fernandes, D. F. Valcarcel, and A. J. N. Batista. Marte: A multiplatform real-time framework. *IEEE Transactions on Nuclear Science*, 57(2):479–486, April 2010.
- [9] G. De Tommasi, F. Piccolo, A. Pironti, and F. Sartori. A flexible software for real-time control in nuclear fusion experiments. *Control Engineering Practice*, 14(11):1387–1393, 2006.
- [10] André C. Neto, Diogo Alves, Luca Boncagni, Pedro J. Carvalho, Daniel F. Valcárcel, Antonio Barbalace, Gianmaria De Tommasi, Horácio Fernandes, Filippo Sartori, Enzo Vitale, Riccardo Vitelli, and Luca Zabeo. A survey of recent MARTe based systems. In *IEEE Transactions on Nuclear Science*, volume 58, pages 1482–1489, 2011.

Bibliography

- [11] A Neto, D Alves, B B Carvalho, P J Carvalho, H Fernandes, D F Valc, G De Tommasi, Associazione Euratom-enea create, Via Claudio, P McCullen, A Stephen, Euratom-ccfe Fusion Association, Culham Science Centre, Abingdon Ox, United Kingdom, R Vitelli, Tor Vergata, Via Politecnico, L Zabeo, and Iter Organisation. Marte Framework : a Middleware for Real-Time Applications Development. In *13th International Conference on Accelerator and Large Experimental Physics Control Systems*, number 11, pages 1277–1280, Grenoble, France, 2011.
- [12] Andre C. Neto, Filippo Sartori, Riccardo Vitelli, Llorenç Capella, Giuseppe Ferro, Ivan Herrero, and Hector Novella. An agile quality assurance framework for the development of fusion real-Time applications. In *2016 IEEE-NPSS Real Time Conference, RT 2016*, 2016.
- [13] Chiara Piron, Gabriele Manduchi, Paolo Bettini, Federico Felici, Claudio Finotti, Paolo Franz, Ondrej Kudlacek, Giuseppe Marchiori, Lionello Marrelli, J. M. Moret, Paolo Piovesan, Olivier Sauter, and Cesare Taliercio. Integration of the state observer RAPTOR in the real-time MARTE framework at RFX-mod. *Fusion Engineering and Design*, 123:616–619, 2017.
- [14] William R. Spears. JT-60SA construction status. *IEEE Transactions on Plasma Science*, 2014.
- [15] JT-60SA Team. Research objectives and strategy. Technical report, 2018. <http://www.jt60sa.org/>.
- [16] N Cruz, G. De Tommasi, M Mattei, A Mele, Y Miyata, A Pironti, and T Suzuki. Control-oriented tools for the design and validation of the JT-60SA magnetic control system. *Control Engineering Practice*, 63:81–90, 2017.
- [17] JT-60SA Team. Plant integration document. Technical report, 2017. <https://users.jt60sa.org/?uid=222UJY>.
- [18] R. Albanese, R. Ambrosino, and M. Mattei. CREATE-NL+: A robust control-oriented free boundary dynamic plasma equilibrium solver. *Fus. Eng. Des.*, 96–97:664–667, Oct. 2015.
- [19] R. Albanese and F. Villone. The linearized CREATE-L plasma response model for the control of current, position and shape in tokamaks. *Nucl. Fus.*, 38(5):723–738, May 1998.
- [20] R. Albanese, G. Ambrosino, M. Ariola, A. Cenedese, F. Crisanti, G. De Tommasi, M. Mattei, F. Piccolo, A. Pironti, F. Sartori, and F. Villone. Design, implementation and test of the XSC extreme shape controller in JET. *Fusion Engineering and Design*, 74(1-4):627–632, 2005.
- [21] H. Anand et al. A novel plasma position and shape controller for advanced configuration development on the TCV tokamak. *Nucl. Fus.*, 57(12):126026, 2017.
- [22] E. de la Luna et al. Recent Results on High-Triangularity H-Mode Studies in JET-ILW. In *26th IAEA Fusion Energy Conference*, Kyoto, Japan, October 2016.
- [23] G. Ambrosino et al. Design and Implementation of an Output Regulation Controller for the JET Tokamak. *IEEE Trans. Control Syst. Tech.*, 16(6):1101–1111, Nov. 2008.

- [24] M. Ariola and A. Pironti. The design of the eXtreme Shape Controller for the JET tokamak. *IEEE Control Sys. Mag.*, 25(5):65–75, Oct. 2005.
- [25] H. Urano et al. Y. Miyata. Documents on inputs, outputs of ccs(cauchy condition surface) method. Technical report, 2018.
- [26] H. Urano et al. Y. Miyata. Documents on inputs, outputs and control scheme of the qst magnetic controller. Technical report, 2018.
- [27] G. De Tommasi et al. Shape Control with the eXtreme Shape Controller During Plasma Current Ramp-Up and Ramp-Down at the JET Tokamak. *J. Fus. Energy*, 33(2):149–157, 2014.
- [28] H. Urano et al. Development of operation scenarios for plasma breakdown and current ramp-up phases in JT-60SA tokamak. *Fus. Eng. Des.*, 100:345–356, 2015.
- [29] H. Meyer et al. Overview of progress in European medium sized tokamaks towards an integrated plasma-edge/wall solution. *Nuclear Fusion*, 57, 2017.
- [30] Y. Miyata et al. Study of JT-60SA Operation Scenario using a Plasma Equilibrium Control Simulator. *Plasma and Fus. Res.*, 8:2405109–2405109, 2013.
- [31] Y. Miyata, T. Suzuki, S. Ide, and H. Urano. Study of Plasma Equilibrium Control for JT-60SA using MECS. *Plasma and Fus. Res.*, 9:3403045–5, 2014.

A

EXTENDED CONTROL RESULTS

This appendix contains the corresponding plots of the ISTTOK discharges from table 5.2.1.

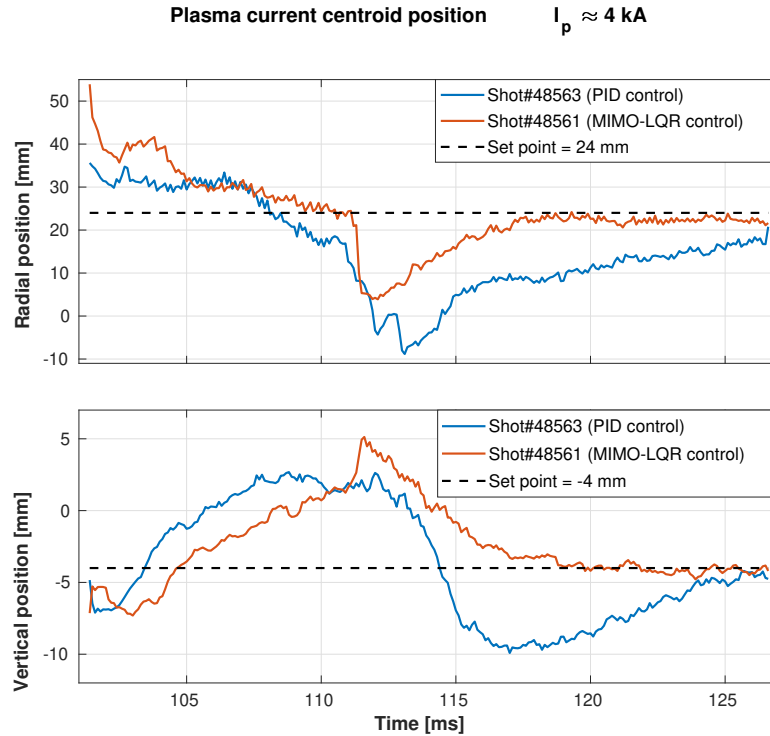


Figure A.1.: Plasma centroid position Shot# 48563 Shot# 48561

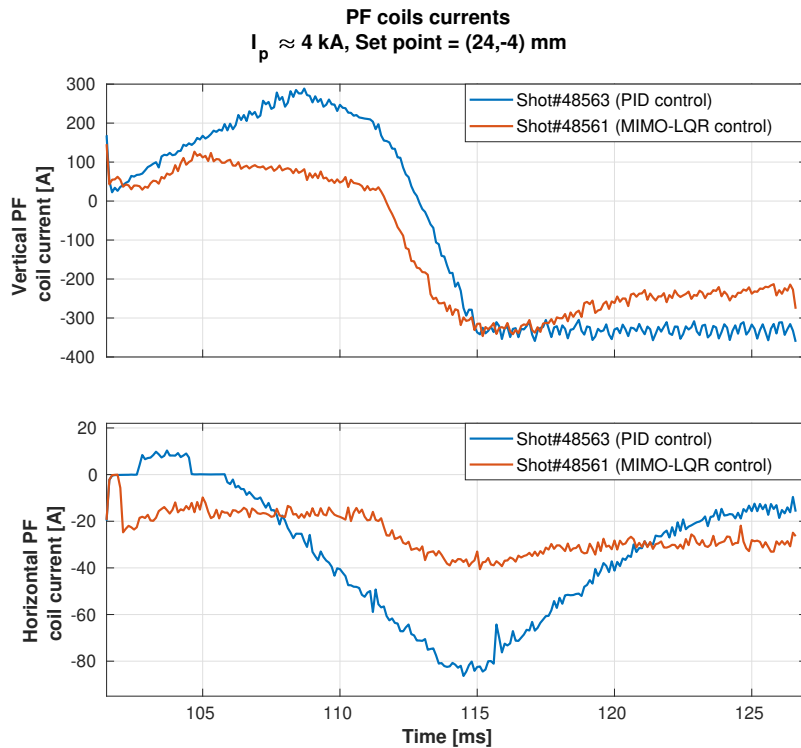


Figure A.2.: lalala Shot# 48563 Shot# 48561

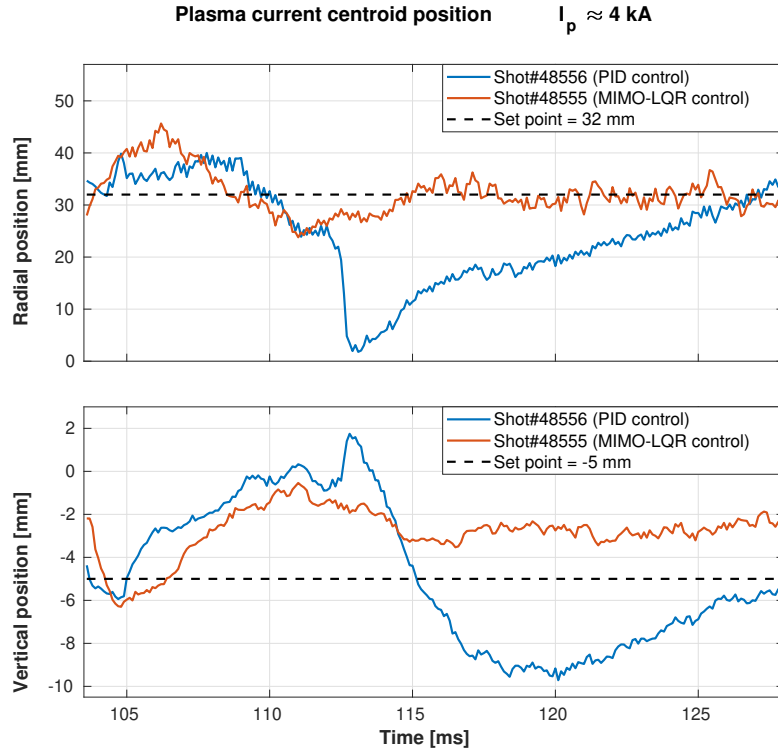


Figure A.3.: Plasma centroid position Shot# 48556 Shot# 48552

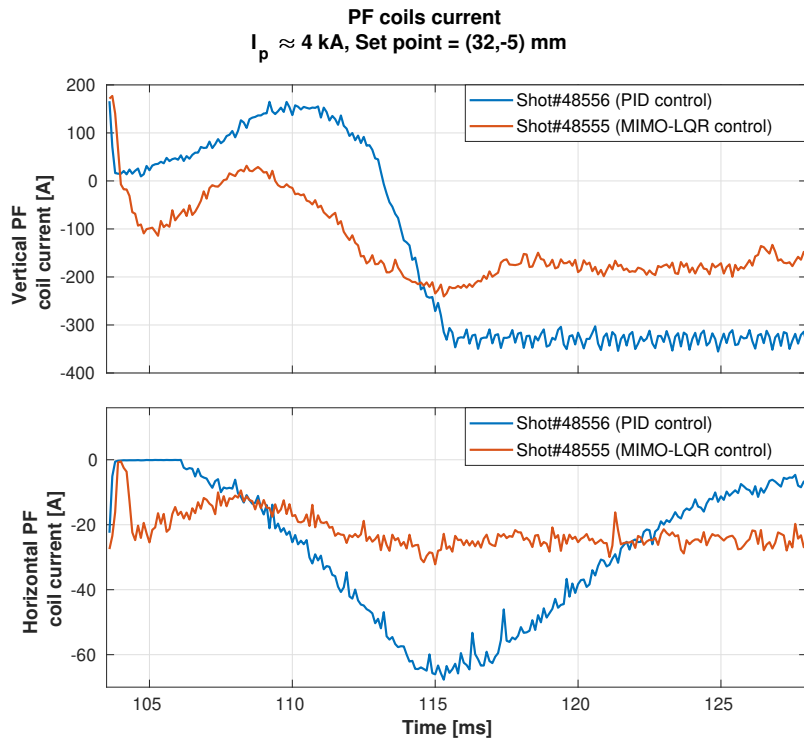


Figure A.4.: lalala Shot# 48556 Shot# 48552

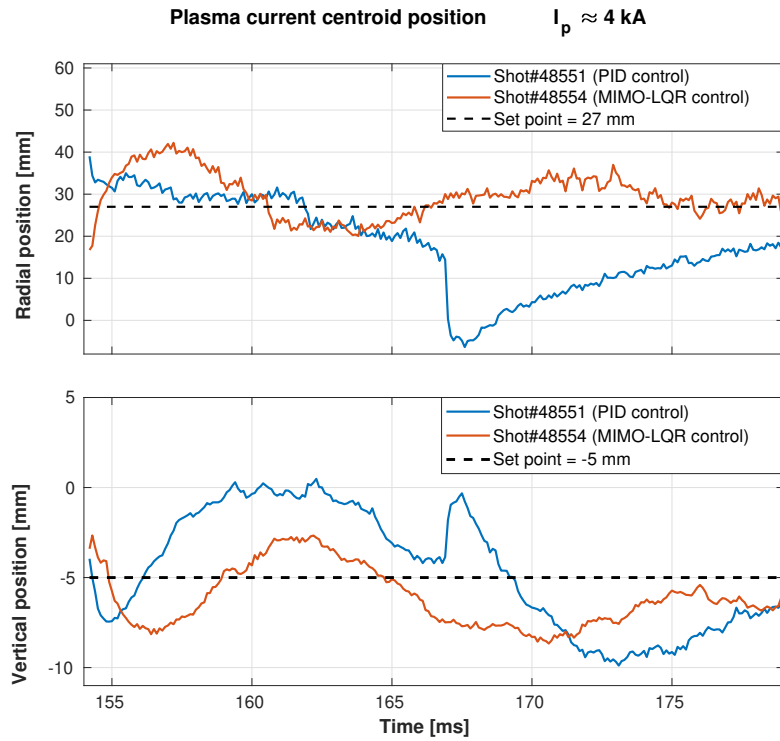


Figure A.5.: Plasma centroid position Shot# 48551 Shot# 48554

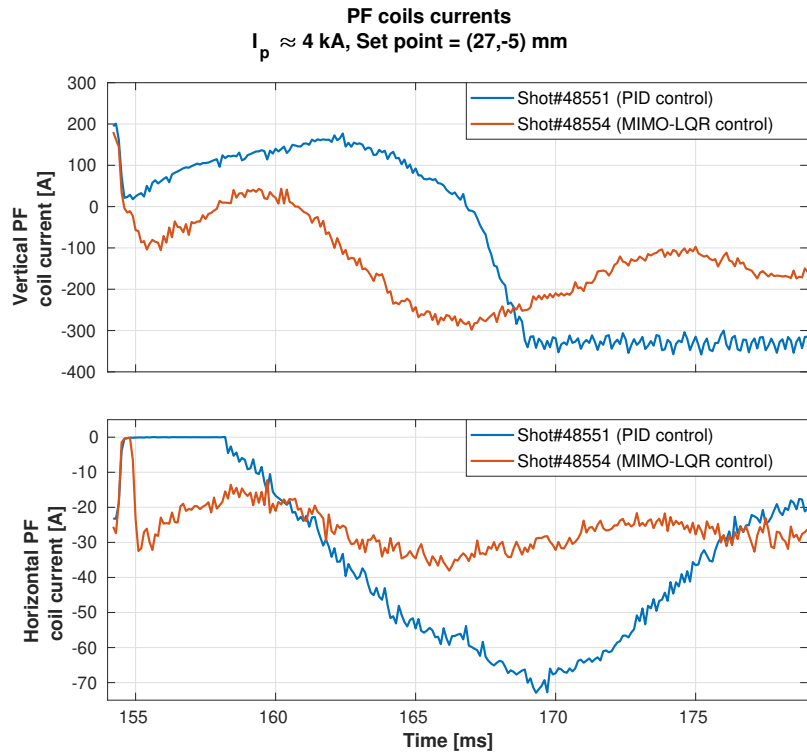


Figure A.6.: lalala Shot# 48551 Shot# 48554

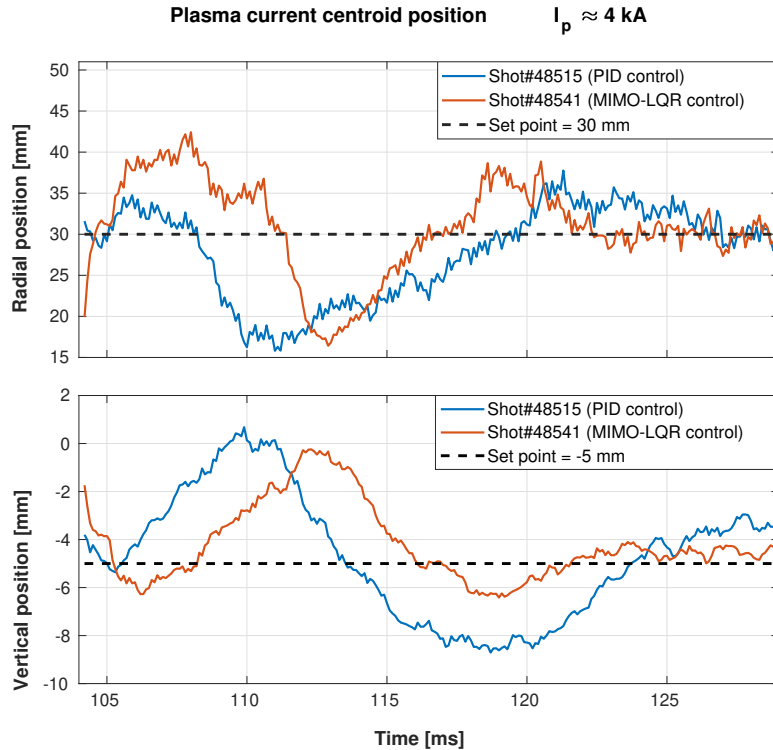


Figure A.7.: Plasma centroid position Shot# 48515 Shot# 48541

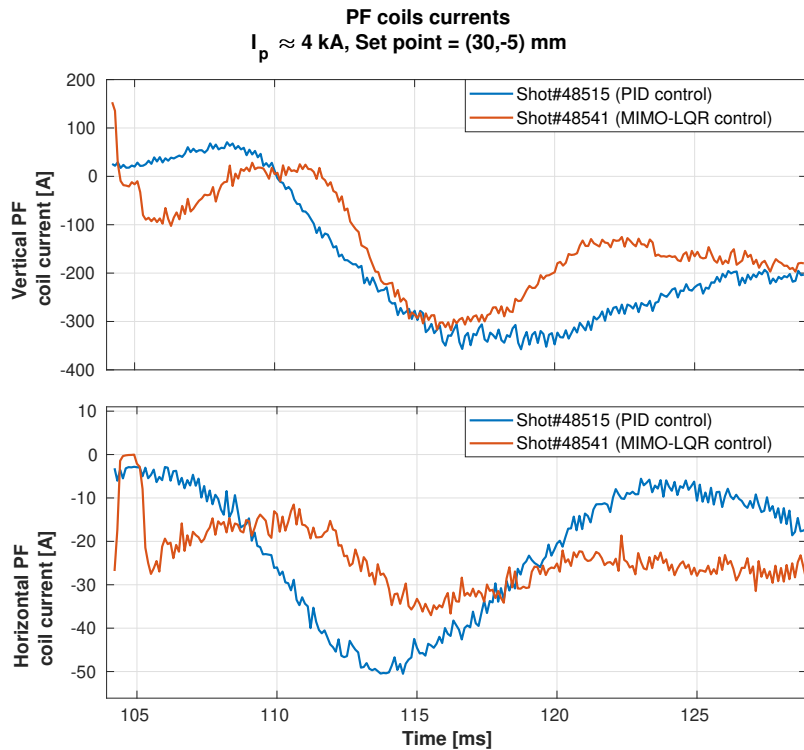


Figure A.8.: lalala Shot# 48515 Shot# 48541

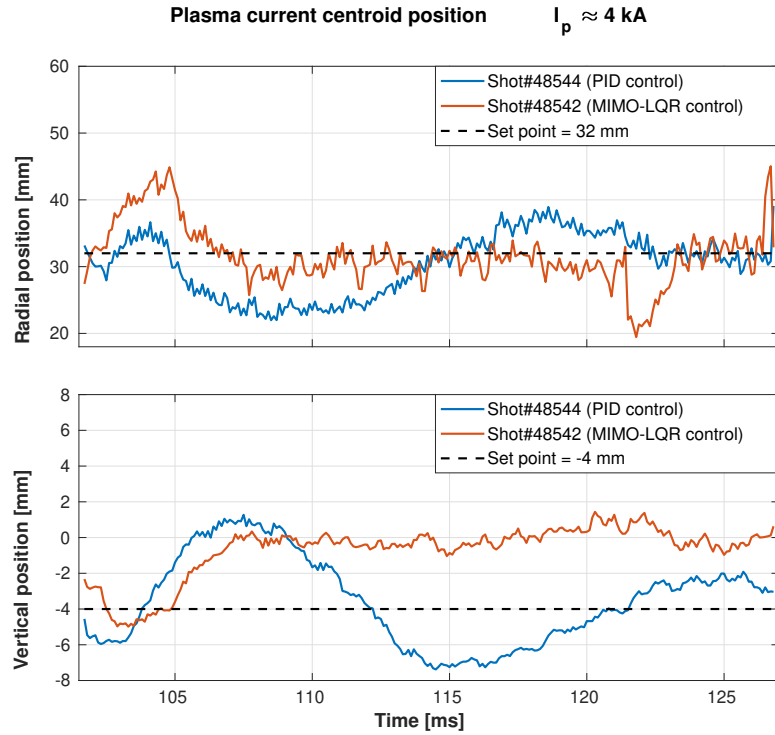


Figure A.9.: Plasma centroid position Shot# 48544 Shot# 48542

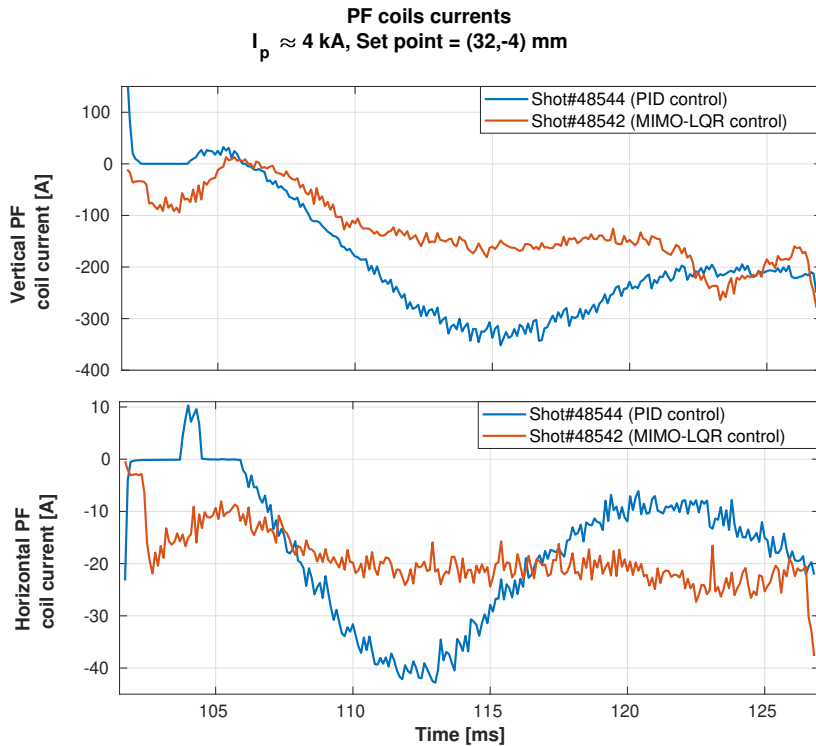


Figure A.10.: lalala Shot# 48544 Shot# 48542

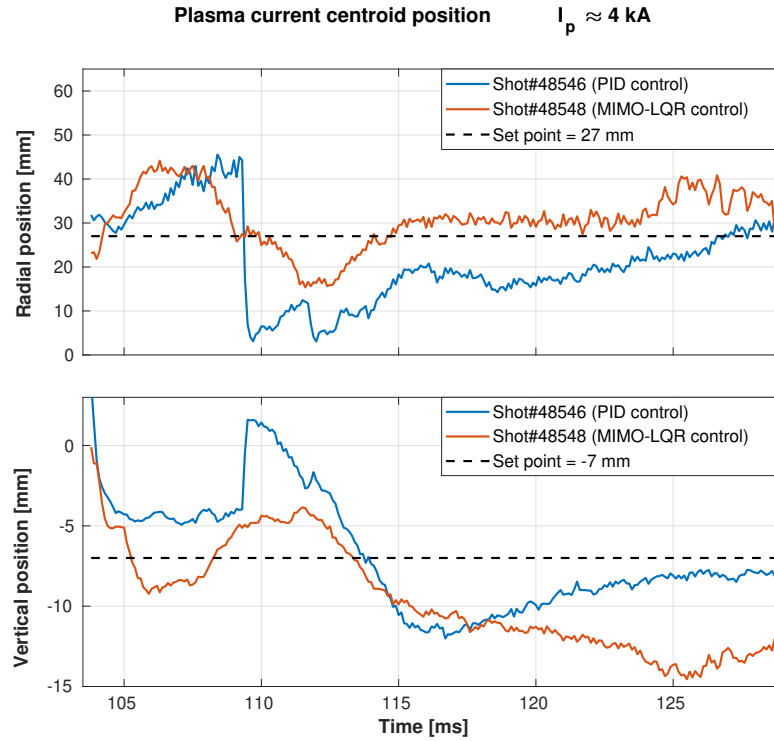


Figure A.11.: Plasma centroid position Shot# 48546 Shot# 48548

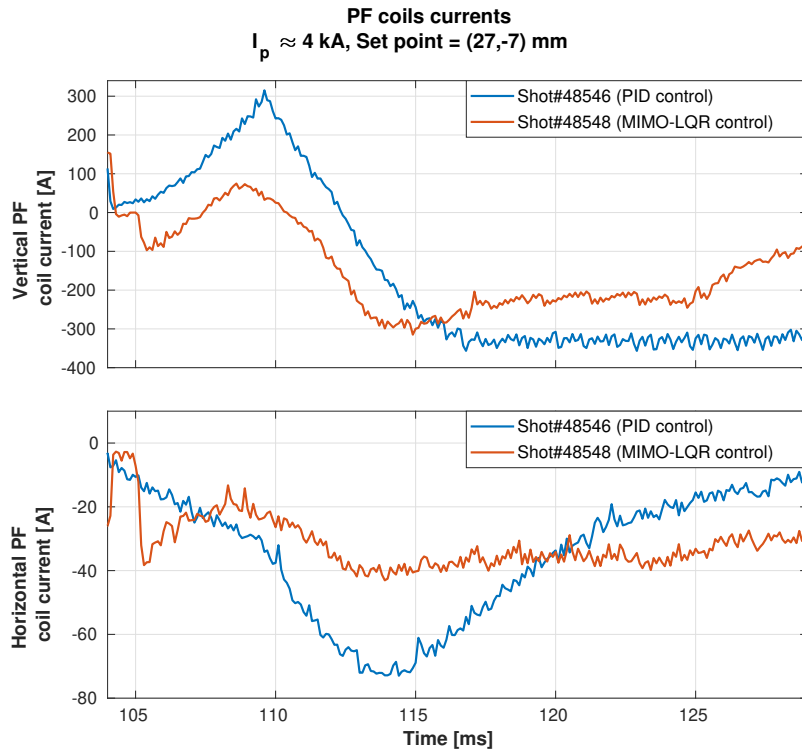


Figure A.12.: lalala Shot# 48546 Shot# 48548

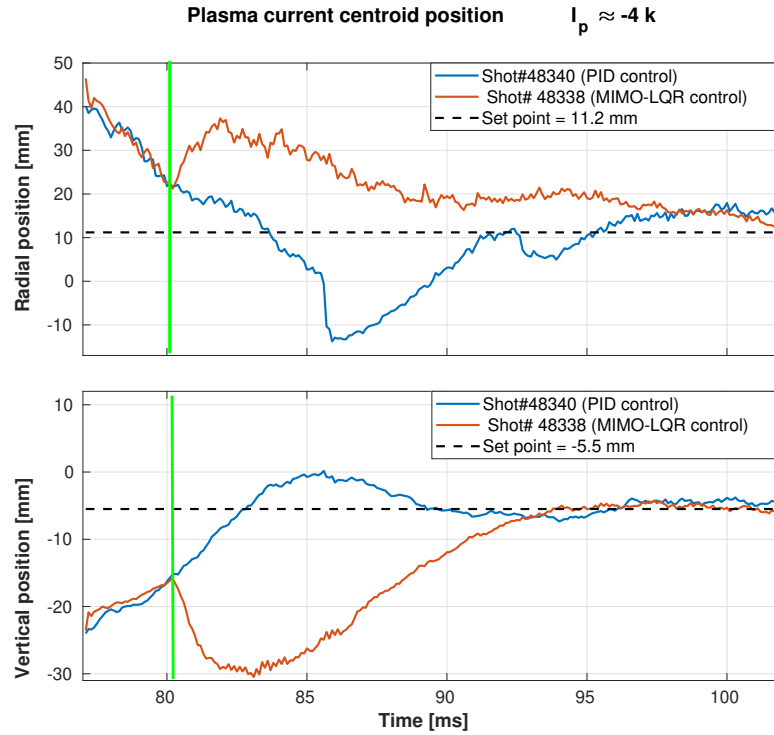


Figure A.13.: Plasma centroid position Shot# 48340 Shot# 48338

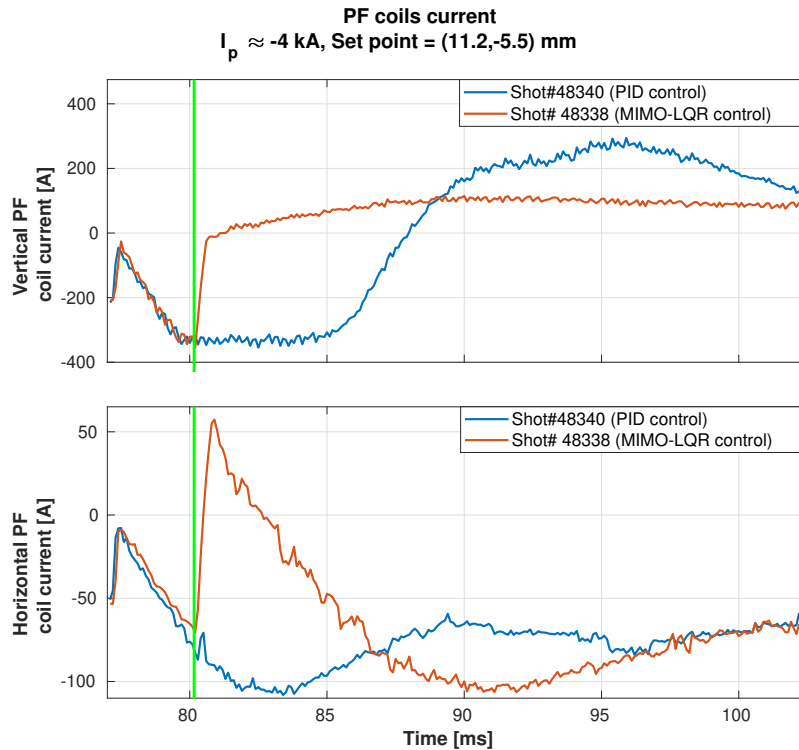


Figure A.14.: lalala Shot# 48340 Shot# 48338

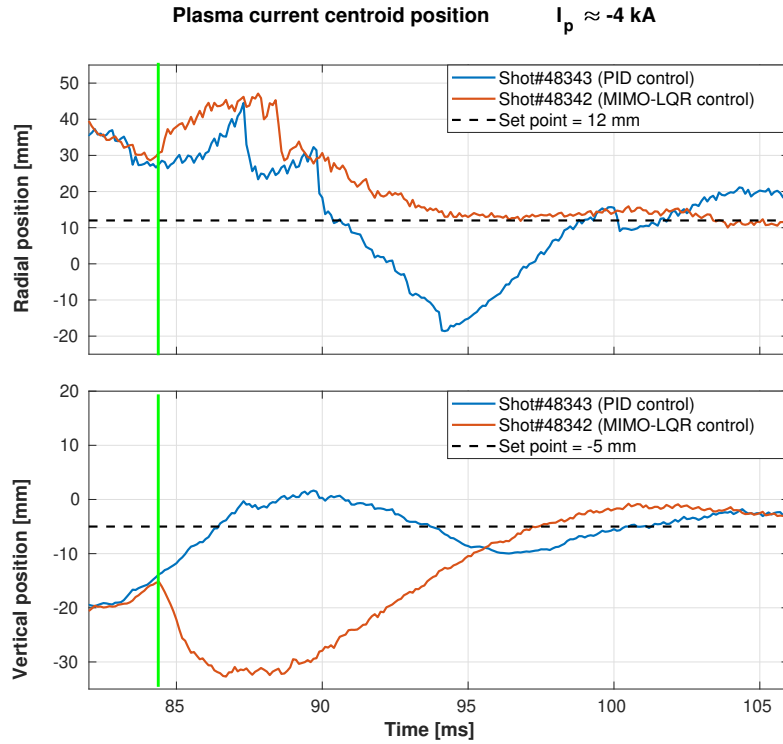


Figure A.15.: Plasma centroid position Shot# 48343 Shot# 48342

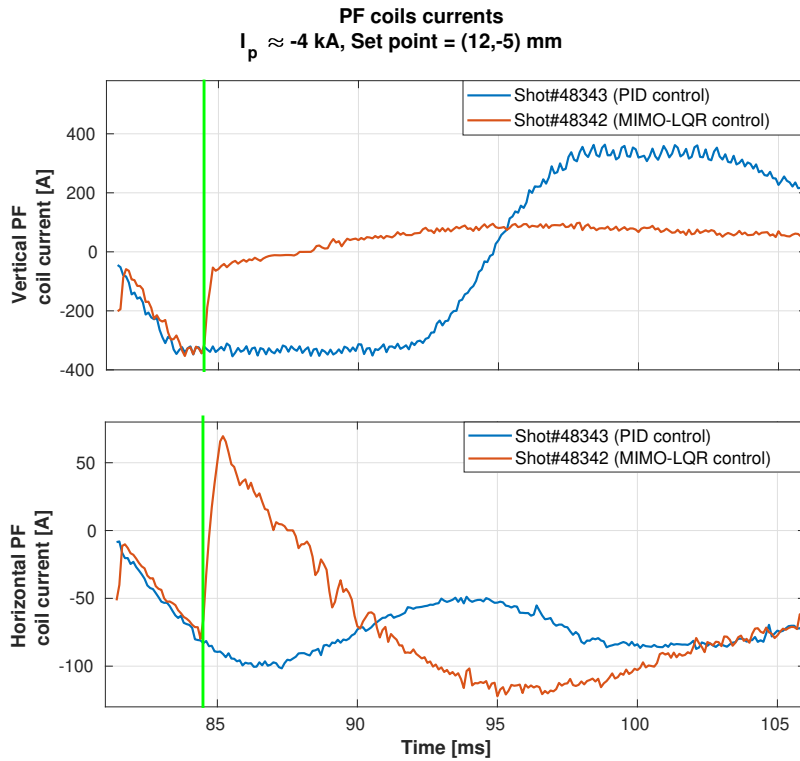


Figure A.16.: lalala Shot# 48343 Shot# 48342

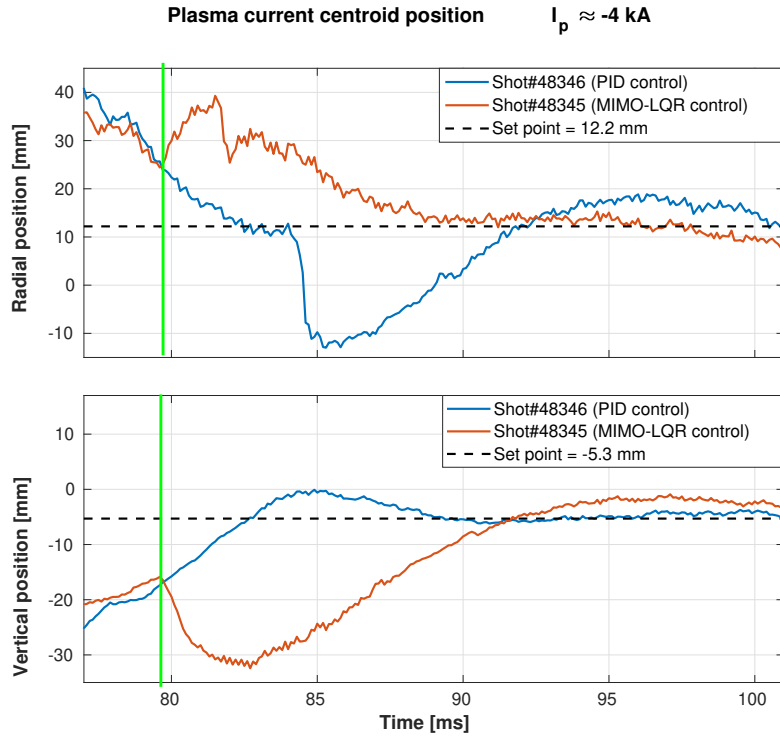


Figure A.17.: Plasma centroid position Shot# 48346 Shot# 48345

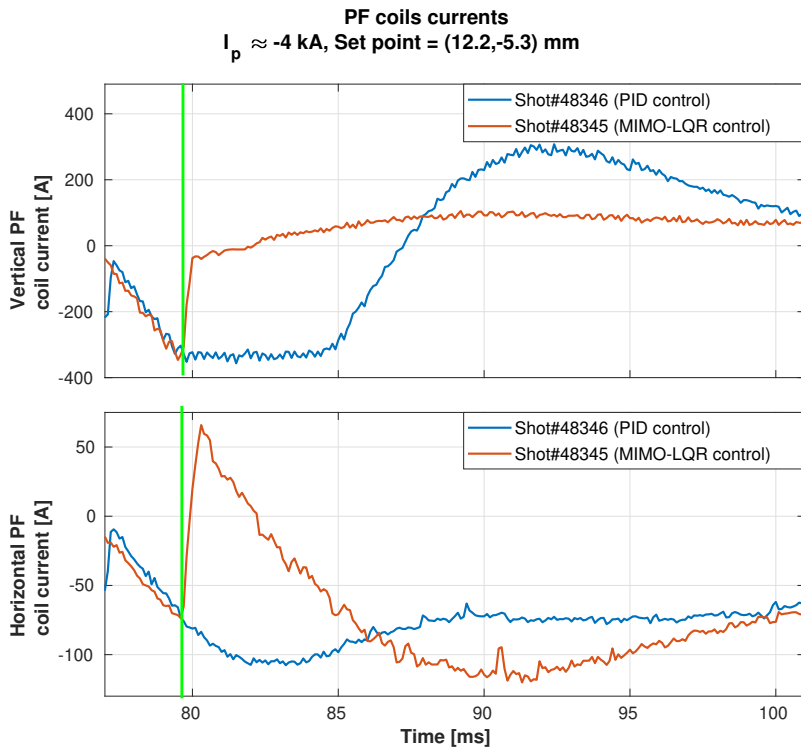


Figure A.18.: lalala Shot# 48346 Shot# 48345

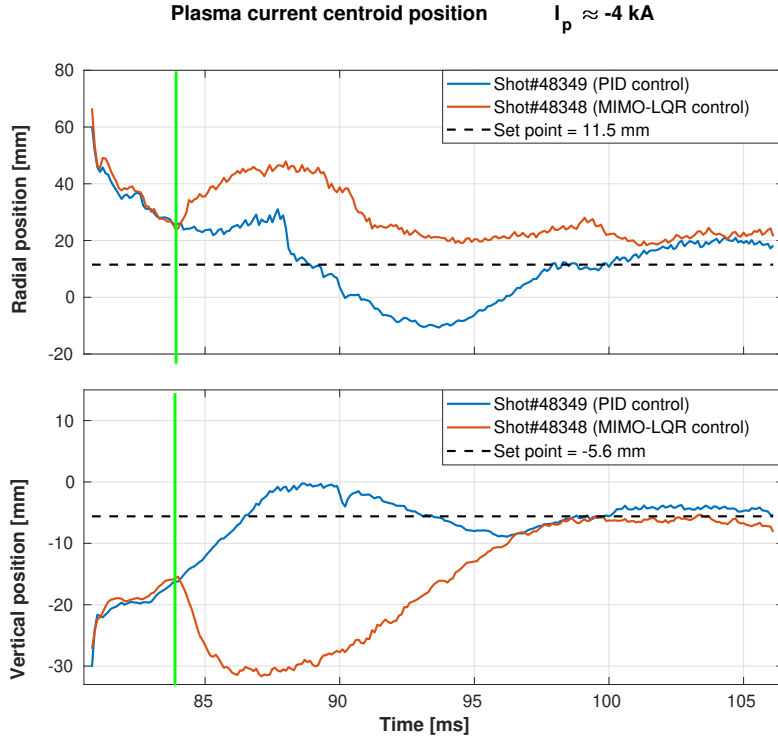


Figure A.19.: Plasma centroid position Shot# 48349 Shot# 48348

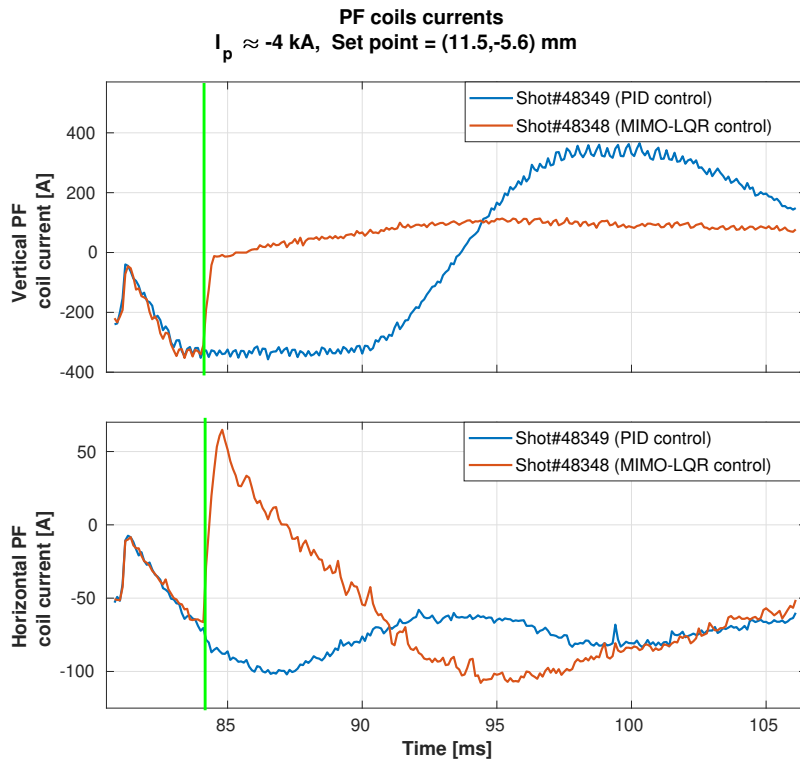


Figure A.20.: lalala Shot# 48349 Shot# 48348

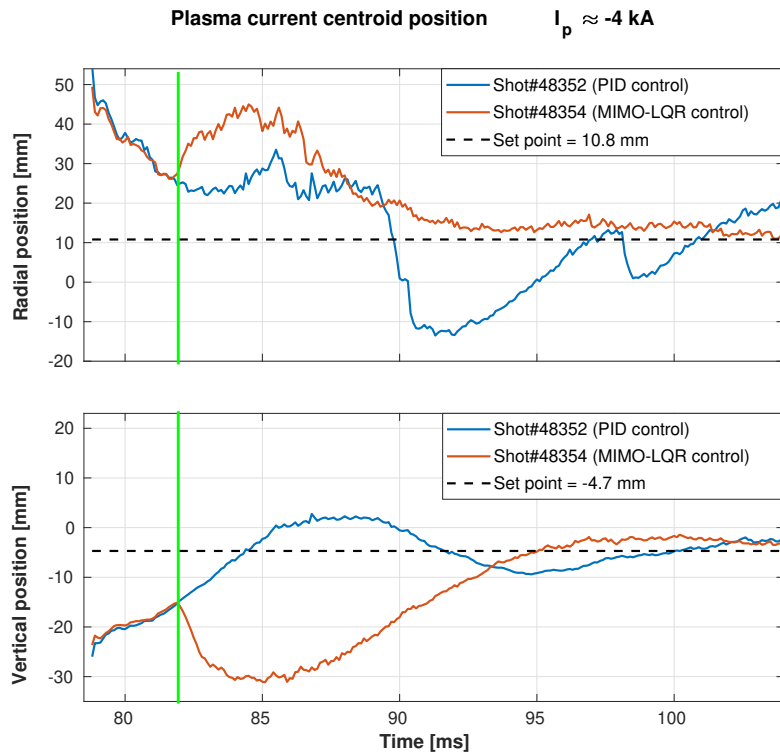


Figure A.21.: Plasma centroid position Shot# 48352 Shot# 48354

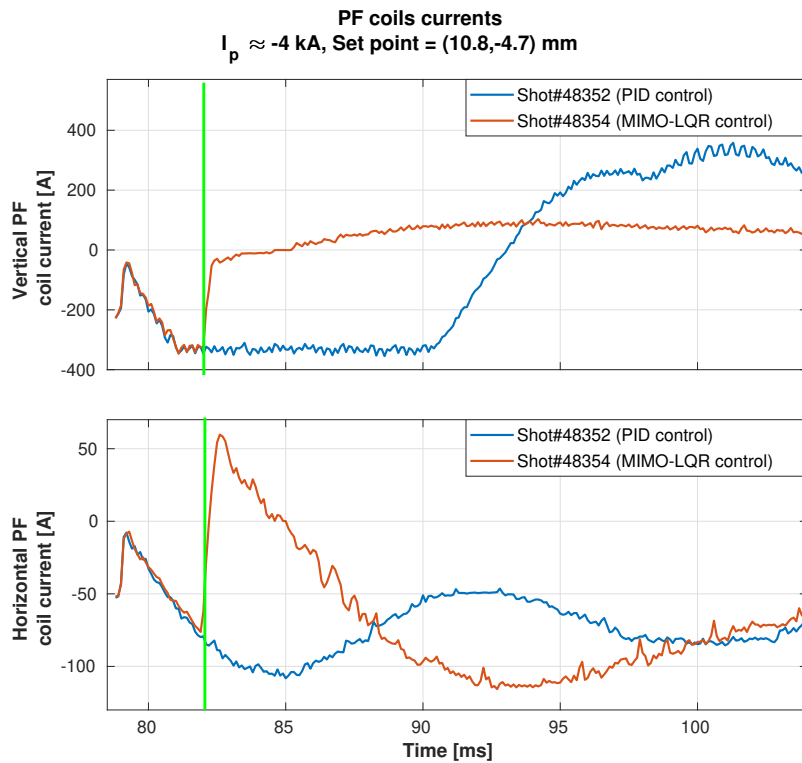


Figure A.22.: lalala Shot# 48352 Shot# 48354

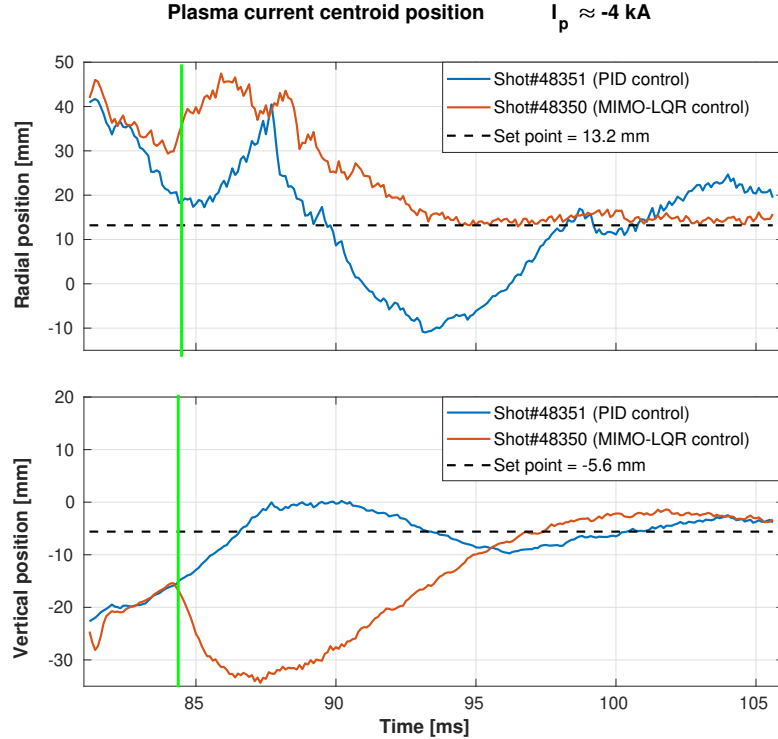


Figure A.23.: Plasma centroid position Shot# 48351 Shot# 48350

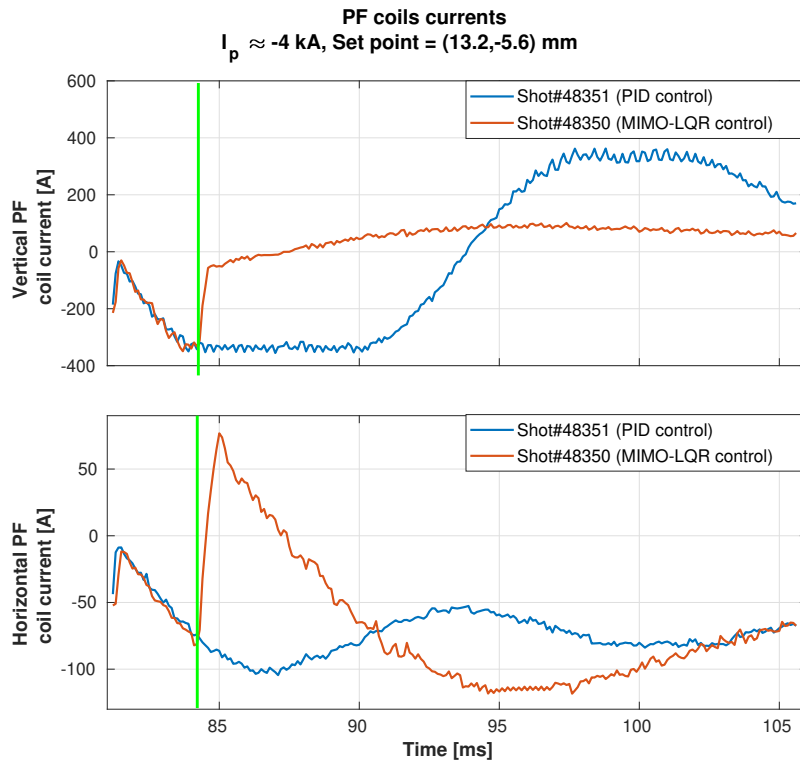


Figure A.24.: lalala Shot# 48351 Shot# 48350

B

FBC CONTROLLER AND CCS CONFIGURATION
